

Non-Thermal Escape of the Martian CO₂ atmosphere over time: Constrained by Ar isotopes

H.I.M. Lichtenegger^a, S. Dyadechkin^a, M. Scherf^{a,*}, H. Lammer^a, R. Adam^b,
E. Kallio^c, U.V. Amerstorfer^a, R. Jarvinen^{c,d}

^a*Space Research Institute, Austrian Academy of Sciences, Graz, Austria*

^b*Institute of Physics, IGAM, Karl Franzens University, Graz, Austria*

^c*Department of Electronics and Nanoengineering, School of Electrical Engineering, Aalto University, Espoo, Finland*

^d*Finnish Meteorological Institute, Helsinki, Finland*

Abstract

The ion escape of Mars' CO₂ atmosphere caused by its dissociation products C and O atoms is simulated from present time to ~ 4.1 billion years ago (Ga) by numerical models of the upper atmosphere and its interaction with the solar wind. The planetward-scattered pick-up ions are used for sputtering estimates of exospheric particles including ³⁶Ar and ³⁸Ar isotopes. Total ion escape, sputtering and photochemical escape rates are compared. For solar EUV fluxes ≥ 3 times that of today's Sun (earlier than ~ 2.6 Ga) ion escape becomes the dominant atmospheric non-thermal loss process until thermal escape takes over during the pre-Noachian eon (earlier than $\sim 4.0 - 4.1$ Ga). If we extrapolate the total escape of CO₂-related dissociation products back in time until ~ 4.1 Ga we obtain a theoretical equivalent to CO₂ partial pressure of more than ~ 3 bar, but this amount did not necessarily have to be present. The fractionation of ³⁶Ar/³⁸Ar isotopes through sputtering and volcanic outgassing from its initial chondritic value of 5.3, as measured in the 4.1 billion years old Mars meteorite ALH 84001, until the present day can be reproduced for assumed CO₂ partial pressures between $\sim 0.2 - 3.0$ bar, depending on the cessation time of the Martian dynamo (assumed between 3.6–4.0 Ga) - if atmospheric sputtering of Ar started afterwards.

*Corresponding author, manuel.scherf@oeaw.ac.at

Keywords: atmospheric loss, hybrid simulation, atmospheric sputtering, hot particles

1. Introduction

The evolution and escape of Mars' CO₂ atmosphere in the context of a higher surface partial pressure and a climate that allowed liquid water on the planet's surface, the so-called “warm and wet” early Mars hypothesis, is one of the great riddles in Solar System science (de Pater & Lissauer, 2015; Jakosky & Phillips, 2001; Hurowitz et al., 2017; di Achille & Hynek, 2010; Lammer et al., 2013, 2018; Palumbo et al., 2020; Scherf & Lammer, 2021). Whether early Mars passed through a phase of a warm and wet climate with a much denser atmosphere during the Noachian eon or was predominantly cold and dry with sporadic warm phases is debated. Recently, several studies suggest that Mars most likely had a dense atmosphere during the Noachian eon, with an approximate surface pressure of at least 0.5 bar (Hu et al., 2015; Jakosky et al., 2018; Kurokawa et al., 2018). Kurokawa et al. (2018) tried to reproduce the present atmospheric ¹⁴N/¹⁵N and ³⁶Ar/³⁸Ar isotope ratios by modeling atmospheric escape and volcanic outgassing and concluded that the present isotope ratios can only be reproduced if the atmospheric pressure had at least a value of ~ 0.5 bar 4 billion years ago. The maximum atmospheric surface pressure at ~ 3.6 Ga was estimated from the size distribution of ancient craters by Kite et al. (2014) based on Mars Reconnaissance Orbiter high-resolution images. These researchers obtained an upper surface partial pressure limit of 0.9 ± 0.1 bar, or 1.9 ± 0.2 bar, if they excluded rimmed circular mesas by interpreting them as erosion-resistant fills or floors of impact craters.

Amerstorfer et al. (2017) applied a sophisticated Monte Carlo model using the atmospheric and ionospheric profiles of Tian et al. (2009) corresponding to 1 (present), 3 (2.3-2.6 Ga), and 10 (3.5-3.8 Ga), times the present solar EUV flux (EUV_⊙) to investigate the escape of suprathermal O and C atoms from the Martian upper atmosphere. These authors studied and discussed different

sources of suprathermal O and C atoms in the thermosphere and their effects related to the varying EUV flux. Depending on the EUV activity of the young Sun, Amerstorfer et al. (2017) estimated that suprathermal atom escape from CO₂-dissociation products results in a CO₂ partial surface pressure between about 0.17 – 0.3 bar at ~ 4 Ga, which is lower than the pressure inferred from the atmospheric $^{36}\text{Ar}/^{38}\text{Ar}$ isotope reproduction attempts by Kurokawa et al. (2018).

In particular at Venus and Mars, whose atmospheres are not protected by an intrinsic magnetic field, the interaction of the solar wind with the upper atmosphere plays an important role for atmospheric erosion over Solar System time scales (G. Luhmann & Kozyra, 1991; Luhmann et al., 1992; Fang et al., 2013; Lammer et al., 2013, 2018). More recently, Dong et al. (2018) modeled the escape of O⁺, O₂⁺ and CO₂⁺ by applying a 3D Mars global ionosphere thermosphere model of Bougher et al. (2015) that includes all the relevant neutral-ion chemistry and the radiative processes together with a 3D Mars multifluid magnetohydrodynamic solar interaction model (Najib et al., 2011; Dong et al., 2014). Similar as in Tian et al. (2009) and Amerstorfer et al. (2017), atmospheric escape rates increase when the solar EUV flux exceeds $\sim 3 \text{ EUV}_{\odot}$. The suprathermal O atom escape rates obtained by Dong et al. (2018) increase from $\sim 10^{25} \text{ s}^{-1}$ (1 EUV_{\odot}) to $\sim 10^{26} \text{ s}^{-1}$ (10 EUV_{\odot}) and are similar to those reported by Amerstorfer et al. (2017). During the same time interval, the O⁺ ion escape rate changed from $\sim 10^{24} \text{ s}^{-1}$ to about 10^{27} s^{-1} , indicating that atmospheric loss for early Mars is primarily controlled by ion escape (Dong et al., 2018). The main reason for this high ion escape rate is the expansion of the upper atmosphere when exposed to fluxes larger than 3 EUV_{\odot} .

Besides O⁺ ion escape, Dong et al. (2018) also modeled the loss of O₂⁺ and CO₂⁺ for a radiation of 10 EUV_{\odot} and obtained escape rates of $\sim 10^{25} \text{ s}^{-1}$ and $\sim 4 \times 10^{24} \text{ s}^{-1}$, respectively. These relatively low values are mainly due to the dissociation of these ions by the high EUV flux, leading to a low abundance of the molecules in the upper atmosphere and an increased escape of its dissociation products (Tian et al., 2009). From the ~ 100 times higher O⁺ ion escape rates

at ~ 4 Ga, Dong et al. (2018) concluded that their results are consistent with Mars having lost much of its atmosphere early in its history, causing the Martian climate to change from a warm and wet environment in the past to its present state. However, this conclusion might be questionable, since this particular study did neither include the escape of carbon-related dissociation products from CO_2 nor were the escape rates compared against realistic volcanic outgassing rates.

For better understanding the total atmospheric escape rates of carbon and oxygen related species during the Noachian, we invoke a 3D global hybrid model (Kallio & Janhunen, 2003; Dyadechkin et al., 2013) for the solar wind interaction with Mars using the cold and hot atmospheric profiles for 1, 3 and 10 EUV_\odot given in Amerstorfer et al. (2017). Based on the O^+ and C^+ ions produced by photoionization of cold and suprathermal O and C atoms, we calculate their escape rates as well as the precipitation of these ions into the upper atmosphere. Upon entering these extended upper atmospheres, they can knock out other atmospheric species by transferring sufficient energy to even allow sputtered particles to leave the planet, while a fraction can also contribute to the density of the hot population.

We investigate the sputter efficiency not only for the main atmospheric species, but also for ^{36}Ar and ^{38}Ar noble gas isotopes which will then be used similar as in Kurokawa et al. (2018) to constrain the atmospheric CO_2 partial surface pressure evolution. Finally, we compare the total atmospheric CO_2 loss rates weighted by the escape of C within realistic volcanic CO_2 outgassing rates.

Section 2 contains a brief overview of how the density of hot particles, produced by chemical reactions in the upper atmosphere, are obtained. In Section 3, the 3D global hybrid solar wind interaction model used to simulate the escape and precipitation of atmospheric ions is described, while Section 4 resumes the sputter model. Section 5 deals with the volcanic outgassing of Ar and in Section 6 the results of the simulation are discussed; Section 7 concludes the work.

2. Bulk atmosphere and hot O and C corona

The background bulk CO₂-dominated atmosphere in the simulation for three different solar EUV fluxes, namely 1, 3, and 10 EUV_☉, consists of O, CO, CO₂, C, and O₂⁺, CO₂⁺, CO⁺, and O⁺ and was adopted from Tian et al. (2009) and corresponds to a solar activity being in-between minimum and maximum activity. The production of suprathermal atoms by various reactions in the upper atmosphere, their motion through the atmosphere up to the exobase (i.e., 220 km for 1 EUV_☉, 370 km for 3 EUV_☉, and 750 km for 10 EUV_☉) and their density profiles above the exobase are simulated by means of a Monte Carlo model. Since this model is presented in detail in Gröller et al. (2010, 2012, 2014) and Amerstorfer et al. (2017), we will only briefly describe the essential features.

We start with a number of source reactions, shown in Table 1, which produce the majority of suprathermal O and C in the upper atmosphere of Mars. At discrete altitudes, we determine the velocity distribution of the reaction prod-

Table 1: Sources of suprathermal O and C atoms.

Source reaction hot O	Source reaction hot C
Dissociative recombination	
$\text{CO}^+ + e \rightarrow \text{C} + \text{O}$	$\text{CO}^+ + e \rightarrow \text{O} + \text{C}$
$\text{CO}_2^+ + e \rightarrow \text{CO} + \text{O}$	$\text{CO}_2^+ + e \rightarrow \text{O}_2 + \text{C}$
$\text{O}_2^+ + e \rightarrow \text{O} + \text{O}$	
Chemical reaction	
$\text{O}_2^+ + \text{C} \rightarrow \text{CO}^+ + \text{O}$	
Photodissociation	
$\text{CO} + h\nu \rightarrow \text{C} + \text{O}$	$\text{CO} + h\nu \rightarrow \text{O} + \text{C}$

ucts for a specific reaction and follow the newly born suprathermal atoms along their path through the thermosphere up to the exobase in the gravitational field of Mars. Through collisions with the background atmosphere, the suprathermal particles lose part of their initial energy on their way, while the collision partners from the background gain energy through such collisions on average and thus may become suprathermal. Total and differential cross sections are used to determine the collision probability and the energy transfer. At the exobase altitude, the energy distribution function of the suprathermal atoms is taken to calculate the exosphere density and the loss rates.

The solar flux for the photodissociation reactions is taken from SUMER/SOHO observations (Curd et al., 2001, 2004), where we have chosen observations from April 20, 1997, for quiet Sun conditions. The data were transferred to the orbit of Mars by dividing the photon flux by the square of the Sun-Mars distance. The atmospheric input profiles are assumed to represent average dayside conditions, thus a solar zenith angle of 60° was taken. To determine the solar flux for the considered solar zenith angle, we use the Chapman function for an isothermal atmosphere. The photodissociation and absorption cross sections are taken from the Photo Rate Coefficient Database provided by Huebner et al. (1992).

The kinetic energy transferred to the reaction products due to the exothermic source reaction is randomly chosen from the energy distribution of the corresponding reaction. The total kinetic energy in the center of mass frame, $E_{\text{tot}} = E_{\text{cm}} + E_{\text{br}} + E_v + E_r$, is used to determine the energy distribution. For dissociative recombination (DR), E_{cm} denotes the energy according to the relative velocity of the ion and the electron in the center of mass frame, and E_{br} is the released energy corresponding to the reaction channel. The vibrational and rotational energies are given by E_v and E_r , respectively. All molecules and atoms are assumed to be in their vibrational and rotational ground states. The total kinetic energy, E_{tot} , is then distributed among the reaction products according to their masses. The components of the ion and electron velocity are taken randomly from a 1D Maxwell-Boltzmann distribution according to the temperature of the ions and the electrons. A similar approach, as described

here for DR, was also used for the other reactions listed in Table 1. More details about the computation of the energies are given in Gröller et al. (2010).

The collisions between hot particles and the neutral background atmosphere can be elastic, inelastic, or quenching. While in elastic collisions the kinetic energy is conserved, in inelastic collisions part of the kinetic energy can be transferred into internal energy, i.e. vibrational energy or electronic excitation. An excited reactant will be de-excited and internal energy will be converted into kinetic energy during quenching collisions. For the treatment of the collisions and the corresponding total and differential cross sections, we adopt the same approach as Gröller et al. (2014).

When hot particles arrive at the exobase, their motion above the exobase is assumed to be collisionless and to be described by ballistic orbits; a fraction of these particles can be ionized, thereby forming an additional flux of precipitating pick-up ions. The neutral density profiles for cold (Tian et al., 2009; Zhao & Tian, 2015), and hot C and O atoms modeled as described above are shown for all EUV flux cases in Fig. 1. It is seen that suprathermal C and O atoms produce highly extended hot atom coronae and are the dominant species for both cases. However, for a 10 times higher EUV flux, the upper atmosphere expands to great distances, because a larger amount of the infrared cooling molecule CO_2 is dissociated, which results in more heating and hence thermospheric expansion. As can be seen from Fig. 1, CO_2 molecules that are not dissociated remain close to the planet for both cases. In the following section we discuss the global hybrid model for the escape and precipitation of C^+ and O^+ ions which are dissociation products of CO_2 molecules from these extended upper atmospheres.

3. Ion escape and precipitation modeling

For the simulation of the solar wind with the Martian atmosphere, a global hybrid model, i.e. a semi-kinetic model, which treats the ions as particles and the electron as a massless fluid, is applied by using the upper atmosphere profiles shown in Fig. 1. Since a detailed description of the hybrid model can be found

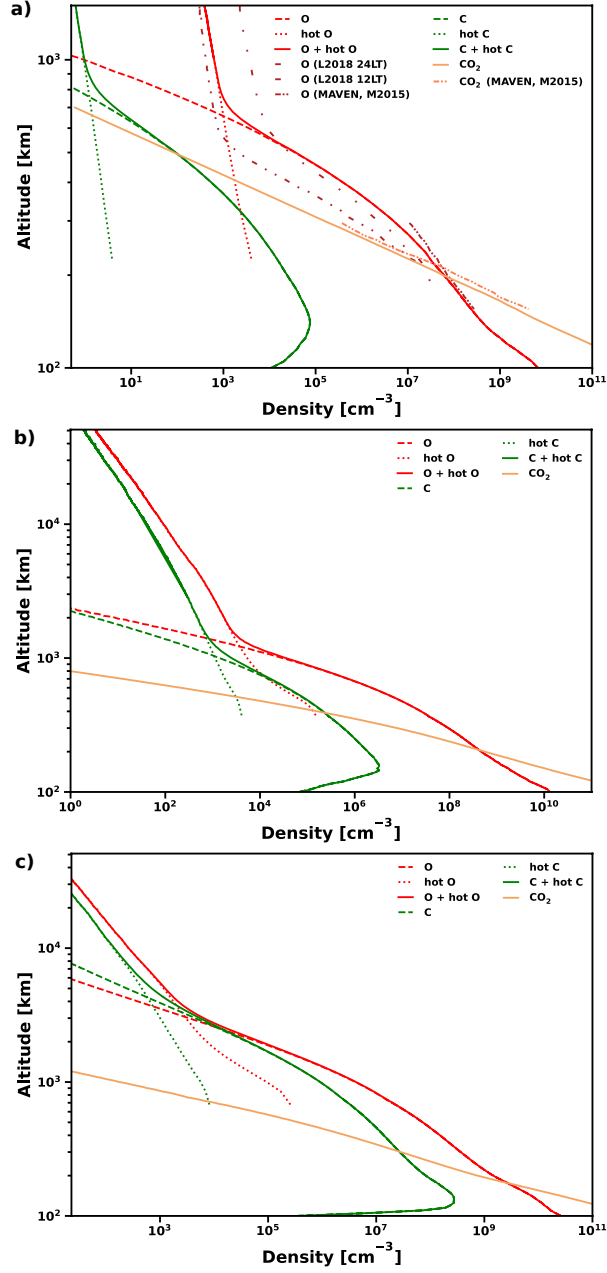


Figure 1: Neutral density profiles of CO₂ molecules and C and O-related dissociation products used in our simulations for present-day (a) and solar EUV fluxes that are 3 times (b) and 10 times (c) enhanced from now. For present-day, we also included MAVEN measurements for O and CO₂, as well as two O profiles from Leblanc et al. (2018) for comparison.

in Kallio & Janhunen (2003) and Dyadechkin et al. (2013), only a brief overview of the model will be given in the following.

3.1. Basic equations of the hybrid model

The hybrid model includes the following equations:

$$\nabla \times \mathbf{B} = \mu_0 \mathbf{j} \quad (1)$$

$$n_e = |e|^{-1} \sum_i q_i n_i \quad (2)$$

$$\mathbf{j} = \sum_i q_i n_i \mathbf{v}_i + en_e \mathbf{U}_e \quad (3)$$

$$\mathbf{E} = -\mathbf{U}_e \times \mathbf{B} + \frac{\nabla p_e}{en_e} + \frac{\mathbf{j}}{\sigma} \quad (4)$$

$$\frac{\partial \mathbf{B}}{\partial t} = -\nabla \times \mathbf{E} \quad (5)$$

$$\frac{d\mathbf{v}_i}{dt} = \frac{q_i}{m_i} \left(\mathbf{E} + \mathbf{v}_i \times \mathbf{B} \right) \quad (6)$$

$$\frac{d\mathbf{x}_i}{dt} = \mathbf{v}_i \quad (7)$$

Equation (1) represents Ampère's law, where \mathbf{B} is the magnetic field, \mathbf{j} is the total electric current density and μ_0 is the magnetic permittivity in a vacuum. Equation (2) states the quasi-neutrality of electric charge, where n_e , e , n_i and q_i are the number density and charge of the electron and ions, respectively. Equation (3) is the total electric current density, i.e. the sum of the electric current of electrons and ions, with \mathbf{v}_i and \mathbf{U}_e being the velocity of the ions and the bulk velocity of the electron fluid, respectively. Equation (4) is generalized Ohm's law, where ∇p_e is the gradient of the electron pressure (assuming an isothermal electron fluid with $p_e = n_e k_B T_e$, where $T_e = 10^5$ K) and σ the electric conductivity. Equation (5) is Faraday's law, while Equation (6) represents Newton's law of motion, including the Lorentz force and with m_i being the mass of the ions. Finally, the last Equation (7) defines the velocity of the ions. In the simulations, the ionospheric obstacle to the solar wind flow is modeled as a superconducting sphere. This is implemented by setting the resistivity at

zero inside the inner boundary and the magnetic field does not diffuse through the obstacle. Further, ions impacting the inner boundary are removed from the hybrid model and are then used as sputter agents at the exobase level in the sputtering model.

3.2. Simulation domain and input parameters

The following right handed cartesian coordinate system was used in the simulations: The x -axis points from the center of the planet against the solar wind flow which is assumed to flow along the Mars-Sun line, the IMF component perpendicular to the solar wind flow is along the y -axis and, thus, the convection electric field is along the z -axis. The size of the simulation box extends from $-15 R_M$ to $15 R_M$, with R_M as the radius of Mars ($R_M = 3390$ km) , in all three coordinate directions with $123 \times 123 \times 123$ grid cells, each having a size of $847.5 \text{ km} = R_M/4$. Mars is assumed to be unmagnetized, the solar wind consists of a single species H^+ and the simulation timestep is 50 ms.

The three global hybrid simulations performed in this study used the same grid cell and simulation domain sizes to keep the model results comparable to each other. This means that the spatial resolution was quite coarse near the inner boundary (see Table 3), which can affect the morphology of the magnetic and electric field at low altitudes. However, the oxygen ion escape and precipitation rates in the 1 EUV_\odot case were found to be close to earlier high-resolution simulations for Mars suggesting that the used spatial resolution does not affect our conclusions (Jarvinen et al., 2018).

In the simulations, the planetary ions are obtained by photoionization (see Table 2) of four different atmospheric populations: cold and hot O, and cold and hot C (see Fig. 1). The photoionization rates in the 1 EUV_\odot case are averages between the Quiet Sun and Active Sun values of the total C and O rate coefficients (three states summed together) in the PHoto Ionization/Dissociation RATES database¹ (Huebner & Carpenter, 1979; Huebner et al., 1992; Huebner

¹<https://phidrates.space.swri.edu>, referenced on April 22, 2021.

& Mukherjee, 2015) scaled from 1 AU to Mars orbital distance. The photoionization rate coefficients in the 3 EUV_☉ and 10 EUV_☉ cases are the 1 EUV_☉ case values multiplied by the factor of 3 and 10, respectively. Hot particles are defined by having an energy $E > 1.5 \times E_{\text{therm}}$ and cold particles by $E < 1.5 \times E_{\text{therm}}$ with E_{therm} being the thermal energy (a detailed discussion on this distinction can be found in Amerstorfer et al. (2017)). Since the cold population is only available up to the exobase, its density has been extrapolated by assuming a Maxwell distribution with the given temperature at the exobase. The densities of the hot particles up to $15 R_M$ are extrapolated by using their actual (non-Maxwellian) distribution function at the exobase.

As inputs for the three global hybrid simulations we fit the retrieved densities by the following functions, i.e.,

1 EUV_☉:

$$\text{Cold O : } n(h) = 1.3252 \times 10^{15} \exp(-1.5425 \times 10^{-5}h) \quad (8)$$

$$\text{Cold C : } n(h) = 1.9586 \times 10^{11} \exp(-1.0476 \times 10^{-5}h) \quad (9)$$

$$\text{Hot O : } n(h) = 3.0158 \times 10^{17} h^{-1.4434} \quad (10)$$

$$\text{Hot C : } n(h) = 2.0487 \times 10^{14} h^{-1.401} \quad (11)$$

3 EUV_☉:

$$\text{Cold O : } n(h) = 2.0 \times 10^{78} h^{-11.4} \quad (12)$$

$$\text{Cold C : } n(h) = 1.0 \times 10^{65} h^{-9.406} \quad (13)$$

$$\text{Hot O : } n(h) = 1.2104 \times 10^{20} h^{-1.7454} \quad (14)$$

$$\text{Hot C : } n(h) = 6.1269 \times 10^{16} h^{-1.3262} \quad (15)$$

10 EUV_☉:

$$\text{Cold O : } n(h) = 1.82 \times 10^{54} h^{-6.92} \quad (16)$$

$$\text{Cold C : } n(h) = 1.55 \times 10^{44} h^{-5.35} \quad (17)$$

$$\text{Hot O : } n(h) = 1.1638 \times 10^{26} h^{-2.5015} \quad (18)$$

$$\text{Hot C : } n(h) = 4.781 \times 10^{22} h^{-2.0841} \quad (19)$$

Table 2: Photoionization rates of oxygen and carbon ions in the global hybrid simulation.

Run	O ⁺ [s ⁻¹]	C ⁺ [s ⁻¹]
EUV 1	5.87×10^{-7}	7.985×10^{-6}
EUV 3	1.761×10^{-6}	2.3955×10^{-5}
EUV 10	5.87×10^{-6}	7.985×10^{-5}

Here, h is the altitude above the surface in m, and $n(h)$ is the particle density in m^{-3} .

Young solar-like stars show a wide variety of different rotation rates which strongly influences their mass loss and EUV flux evolution (Tu et al., 2015; Johnstone et al., 2015b,a). Even though solar-like stars start with similarly high EUV flux and mass loss rates, the irradiation and stellar winds of slow rotators decline much faster than for moderate or even fast rotators. After about one billion years, however, all stars converge again towards one common rotational track. For our simulations, we assumed the Sun to be born as a slow rotator which is in agreement with several recent studies (e.g. Saxena et al., 2019; Lammer et al., 2020a). Therefore, our model runs for 3 and 10 EUV_⊙ correspond to about 2.6 and 3.8 Ga, respectively, (Tu et al., 2015; Amerstorfer et al., 2017).

For estimating the solar wind parameters (see Table 3), i.e. the interplanetary magnetic field B_{IMF} , solar wind temperature T_{sw} , velocity V_{sw} and density n_{sw} , we use the 1D thermal pressure driven hydrodynamic stellar wind evolution model for low-mass main-sequence stars developed by Johnstone et al. (2015a). The model is calibrated with present-day solar wind data and assumes that the mass loss rate \dot{M}_\star depends on the rotation rate Ω_\star as $\dot{M}_\star \propto \Omega_\star^a$ with $a \sim 1.33$ (Model A of Johnstone et al., 2015b) while the wind temperature scales linearly with the coronal temperature.

Even though we aligned our model runs to the evolution of a slow rotator, the results can be easily adapted for moderate and fast rotators, since the

only parameter that changes significantly is the time in the past for which the EUV flux of the Sun coincides with 3 and 10 EUV_⊙. The solar wind parameter themselves, however, vary insignificantly for the same EUV fluxes within different rotational tracks.

Table 3: Simulation parameters

EUV level	B_x	B_y	B_z	n_{sw} [cm ⁻³]	V_{sw} [km/s]	T_{sw} [K]	T_{exo} [K]	exobase altitude [km]	hybrid model inner boundary [km]
1	0	1.08	0	1.83	475.8	5.5×10^4	222	220	300
3	0	1.81	0	2.54	574.8	7.3×10^4	416	370	370
10	0	2.93	0	3.42	693.9	9.7×10^4	806	750	850

4. Atmospheric sputtering

The estimation of the atmospheric sputter yields caused by the precipitating pick-up O⁺ and C⁺ ions is based on the model of Johnson (1990, 1994). The sputter yield Y_i , i.e. the number of species i ejected per incident ion, basically consists of two contributions: the ejection of particles by a single collision with the incoming ion, Y^s , and the ejection due to the cascade of collisions initiated by the incoming ion, Y^c , approximated by (Johnson, 1990)

$$Y^s \approx \bar{P}_{es}^i \frac{\sigma(T > U_{0i})}{\sigma_d(E_{es}) \cos \theta}, \quad Y^c \approx \frac{\beta}{2} \frac{\alpha S_n(E_{in})}{U_{0i} \sigma_d(E_{es})} \frac{1}{(\cos \theta)^p}. \quad (20)$$

Here, \bar{P}_{es}^i is the escape probability for species i , $\sigma(T > U_{0i}) \equiv \int_{U_{0i}} d\sigma$ is the collision cross section for a particle receiving an energy transfer T sufficiently high to enable escape, where U_{0i} is the gravitational binding energy of species i at the exobase, $\sigma_d(E_{es})$ is the momentum cross section of species i escaping with energy E_{es} , and θ is the polar angle of the incident ion. Further, S_n is the nuclear stopping cross section, expressed by (Johnson, 1990),

$$S_n = \frac{\gamma E_{in}}{2} \sigma_d(E_{in}), \quad \gamma = \frac{4m_{in}m_{es}}{(m_{in} + m_{es})^2}, \quad (21)$$

where m_{in} and m_{es} are the masses of the incident and escaping particle, respectively, and where the parameter α depends on the mass ratio m_{es}/m_{in} , β on the interaction potential, and p mainly on the energy of the precipitating ions.

Finally, the cross section for transferring an amount of energy between E and $E + dE$ to an initially stationary atom can be written as (Sieveka & Johnson, 1984)

$$\frac{d\sigma}{dE} = \frac{\varepsilon^2}{E_{max}} \frac{d\sigma}{dt}, \quad (22)$$

with the scaled energy transfer t given by (Johnson, 1990),

$$t = \varepsilon^2 \frac{E}{E_{max}}, \quad E_{max} = \gamma E_{in}, \quad \varepsilon = \frac{\gamma E_{in} a_u}{2A}, \quad A = \frac{2m_{in}}{m_{in} + m_{es}} Z_{in} Z_{es} e^2, \quad (23)$$

where a_u is the screening radius, Z_{in} and Z_{es} are the nuclear charge of the incident and escaping particle, respectively, and e the electron charge.

Using Gaussian units and a universal interaction potential, the screening radius and the nuclear stopping cross section can be approximated via (Johnson, 1990)

$$a_u = \frac{0.8853 a_0}{Z_{in}^{0.23} + Z_{es}^{0.23}}, \quad S_n = 2\pi \frac{A^2}{\gamma E_{in}} [2\varepsilon s_n(\varepsilon)], \quad (24)$$

where

$$[2\varepsilon s_n(\varepsilon)] = \begin{cases} \ln \varepsilon & \varepsilon > 30 \\ \ln(1 + 1.138 \varepsilon) / (1 + 0.0132 \varepsilon^{-0.787} + 0.196 \varepsilon^{0.5}) & \varepsilon < 30 \end{cases} \quad (25)$$

and with

$$\frac{d\sigma}{dt} = \frac{\pi a_u^2}{2} \frac{f(t^{1/2})}{t^{3/2}}, \quad f(\varepsilon) = \frac{d}{d\varepsilon} [\varepsilon s_n(\varepsilon)]. \quad (26)$$

Using 'standard' values for the parameters α, β and p (Johnson, 1994), the total sputter yield of species i can then be written as

$$Y_i = c_i (Y^s + Y^c) = \frac{c_i}{\sigma_d(\bar{E}_{es})} \left[\frac{0.5 \sigma_A(T > U_{0i})}{\cos \theta} + \frac{3}{\pi^2} \frac{\alpha S_n(E_{in})}{(\cos \theta)^{1/6} U_{0i}} \right], \quad (27)$$

with c_i the concentration of species i at the exobase and \bar{E}_{es} the escape energy averaged over the distribution of escape energies, where the latter is approximated by (Sieveka & Johnson (1984))

$$f(E) \propto \frac{1}{E^2} \left(1 - \sqrt{\frac{E}{\gamma E_{in}}} \right). \quad (28)$$

Although sputtering can potentially eject any atmospheric species residing at the exobase, it is especially interesting to investigate its influence on ^{36}Ar

and ^{38}Ar isotopes. Argon has one of the highest ionization thresholds (e.g., Zahnle et al., 2019) and, similar as CO_2 , a high escape energy, thus a mass-related escape of argon isotopes and hence its fractionation can only be caused by sputtering from precipitating pick-up ions (Jakosky et al., 2017). Consequently, the escape of the atmospheric argon content on Mars after cessation of its magnetic dynamo should solely depend on sputtering. Replicating the loss of argon over time would therefore allow us to constrain possible pathways for the atmospheric development of Mars.

The Martian meteorite ALH84001 with an age of ~ 4.1 billion years (Lapen et al., 2010) encloses isotopic imprints of the ancient Martian atmosphere. Its $^{36}\text{Ar}/^{38}\text{Ar}$ ratio of ~ 5.3 (Mathew & Marti, 2001) is higher than the current Martian atmospheric value of 4.2 ± 0.1 (Atreya et al., 2013) but similar to the value of the Earth’s present-day atmosphere of $^{36}\text{Ar}/^{38}\text{Ar} = 5.32 \pm 0.33$ (Marty, 2012). This decrease of the ratio over time suggests that sputtering preferentially removed the lighter ^{36}Ar isotope from the upper atmosphere. The reason for this preference comes from the diffusive separation of species occurring between the homopause and exobase (Wallis, 1989; Bauer & Lammer, 2004; Lammer et al., 2013). Above the homopause level, turbulent mixing becomes increasingly less efficient until gravity dominates and diffusion sets in. Hence, lighter atoms and molecules become more abundant with height than heavier ones. Since escape occurs at the exobase, lighter particles are therefore preferably removed. The ratio R of the abundances of two species at the exobase to that at the homopause can be written as (Jakosky et al., 1994)

$$R = \exp\left(-\frac{\Delta m g \Delta z}{kT}\right), \quad (29)$$

where Δm is the difference in mass between a lighter and a heavier atom or molecule (e.g. CO_2 and ^{36}Ar , ^{38}Ar), Δz is the difference between the homopause and the exobase altitude, g is the gravitational acceleration, and T is the average temperature at this distance.

To estimate the abundance of both ^{36}Ar and ^{38}Ar isotopes at the exobase level we apply this approach to the atmospheric profiles shown in Fig. 1 and

discussed in Section 2. As these argon isotopes make up only a small fraction of the Martian atmosphere and sputtering is, to first order, only dependent on the relative concentration at the exobase and the necessary escape energy of the species, the sputter loss can be scaled to the loss of the dominant species CO_2 (Johnson et al., 2000).

Hutchins & Jakosky (1996) proposed to calculate the evolutionary loss L_{sp}^i of ^iAr through sputtering via the relation

$$L_{\text{sp}}^i = [\text{CO}_2]_{\text{sp}} \frac{Y(^i\text{Ar}_{\text{hp}})}{Y(\text{CO}_{2,\text{hp}})} \left[\frac{^i\text{Ar}}{\text{CO}_2} \right]_{\text{hp}} R_{^i\text{Ar}/\text{CO}_2} s_{\text{f}}, \quad (30)$$

with $[\text{CO}_2]_{\text{sp}}$ being the amount of CO_2 sputtered per time unit, $Y(^i\text{Ar})/Y(\text{CO}_2)$ represents the ratio of the sputtering yield and $[^i\text{Ar}/\text{CO}_2]_{\text{hp}}$ is the mixing ratio of ^iAr at the homopause, with present day values taken from MAVEN measurements (Jakosky et al., 2015); the factor s_{f} allows to take into account possible uncertainties that are related to the sputter escape estimates. $\text{CO}_{2,\text{hp}}$ is calculated from the partial CO_2 surface pressure P_{CO_2} at each time-step (Leblanc et al., 2012; Slipski & Jakosky, 2016; Kurokawa et al., 2018) with the simple relation

$$\text{CO}_{2,\text{hp}} = \frac{4\pi P_{\text{CO}_2} R_{\text{M}}^2}{m_{\text{CO}_2} g}, \quad (31)$$

where m_{CO_2} is the mass of CO_2 . This approach is valid since 99% of the atmospheric mass is located in the homosphere and the abundance in the upper atmosphere has only a negligible effect on the surface pressure. Additionally, Equation (30) actually only requires the ratio of the argon isotopes to CO_2 at the homopause, which due to efficient mixing is equivalent to the ratio found in the entire homosphere.

We will calculate argon sputtering through both methods, i.e. through the simple scaling with CO_2 sputtering and CO_2 pressure (Equation 30) and directly through calculating how many argon particles are sputtered by the precipitating C^+ and O^+ ions as retrieved from our hybrid simulations. For both calculation methods, we use the yields, as estimated with Equations (20–28). The first method has the advantage that it can give us an initial CO_2 pressure range

for which the $^{36}\text{Ar}/^{38}\text{Ar}$ ratio at 4.1 Ga can be reproduced, but with argon sputtering being simply scaled to CO_2 sputtering and not directly estimated from the precipitating ions that are retrieved from our hybrid simulations. The second method, on the other hand, calculates argon sputtering directly, but cannot give a range for the initial pressure.

5. Volcanic outgassing of argon isotopes and crustal production

Volcanic outgassing has been an important source of atmospheric constituents over most of Mars' history (Jakosky & Phillips, 2001; Manning et al., 2006; Grott et al., 2011, 2013). Here we assume, as in Morschhauser et al. (2011), that part of the mantle undergoes partial melting and produces a new crust on the surface, while releasing volatiles into the atmosphere. We use the following relation from Leblanc et al. (2012) and Slipski & Jakosky (2016) for the estimation of the outgassed Ar isotopes,

$$S_{\text{out}}^i(t) = \frac{{}^iAr_{\text{m}}F_{\text{c}}(t)}{V_{\text{m}}(t)}(t)v_{\text{f}}. \quad (32)$$

Here, $F_{\text{c}}(t)$ denotes the crustal production rate, i.e., how much volume of the mantle is added to the crust per time unit, $V_{\text{m}}(t)$ is the total mantle volume and ${}^iAr_{\text{m}}$ is the abundance of the argon isotope i in the mantle. The additional factor v_{f} can be used to scale the efficiency of this process, since the volcanism rate, ratio of intrusive to extrusive volcanism, enrichment of the argon isotopes and other factors influencing the outgassing are not perfectly constrained. According to Slipski & Jakosky (2016) and based on the implemented crustal production rates F_{c} of Greeley & Schneid (1991) (later than ~ 3.8 Ga) and Morschhauser et al. (2011) (earlier than ~ 3.8 Ga), the factor v_{f} lies within 0.3-1.0. The specific evolution of the argon isotope abundances can then be calculated via

$$\frac{d^iAr}{dt} = S_{\text{out}}^i(t) - L_{\text{sp}}^i(t), \quad (33)$$

where the source term S_{out}^i is the outgassed amount of ${}^i\text{Ar}$ and L_{sp}^i is the sputter loss of ${}^i\text{Ar}$. The total change will be evaluated at each time-step, starting

from the time range when the Martian magnetic field is thought to have ceased between 3.6 Ga and 4.1 Ga (Milbury et al., 2012; Lillis et al., 2013; Mittelholz et al., 2020) until the present-day.

Since the $^{36}\text{Ar}/^{38}\text{Ar}$ ratio of ALH 84001 of ~ 5.3 is comparable to that of carbonaceous chondrites (Marty, 2012; Mazor et al., 1970), no significant fractionation prior to its creation could have occurred. The lack of any fractionation earlier than ~ 4.1 Ga might either be due to the Martian intrinsic magnetic field preventing fractionation through sputtering and/or due to a complete loss of the whole atmosphere prior to ~ 4.1 Ga and a subsequent replenishment through volcanic outgassing or impact delivery. The latter argument is supported by the isotopic ratio of $^{14}\text{N}/^{15}\text{N}$ in ALH 84001, which shows no significant deviation from the chondritic value (Avice & Marty, 2020), while the present-day ratio is much lower, indicating non-thermal escape processes of nitrogen after the formation of the meteorite, such as dissociative recombination of N_2^+ as shown by Fox & Hać (1997). We note however, that, contrary to argon, nitrogen could have also been fractionated due to its lighter weight through ion escape or even thermal loss (see e.g. Lammer et al., 2020b, for a discussion on fractionation through different escape processes) at the time when Mars still maintained its intrinsic magnetic field. The lack of any notable fractionation prior to 4.1 Ga, therefore, supports the idea that Mars lost its entire atmosphere early on (Scherf & Lammer, 2021).

Since our estimated sputtering rates are based on the modeled planetward-scattered exospheric ion flux, we also know the total related escape rate from C^+ , CO^+ , CO_2^+ , O^+ , etc. Because of this, we can then analyze scenarios for which the present day atmospheric $^{36}\text{Ar}/^{38}\text{Ar}$ isotope ratio can be reproduced in dependence on the maximum possible loss of the planet’s CO_2 atmosphere over time, including the role of volcanic outgassing during Mars’ history.

6. Results and Discussion

The global hybrid simulation runs for the three EUV cases are illustrated in Fig. 2. In all the runs, the induced magnetosphere is evident with the bow shock as the outermost boundary, where the flux increases suddenly. Downstream of the bow shock is the turbulent magnetosheath, which separates the induced magnetospheric boundary and the low density wake from the bow shock and the upstream solar wind. In the nominal 1 EUV_☉ run, the induced magnetosphere is the most compact and the bow shock closest to the planet. The size of the induced magnetosphere and the bow shock distance increase in concert with the increasing EUV flux. In the 10 EUV_☉ run, the induced magnetosphere is considerably larger compared to the 1 and 3 EUV_☉ runs. The EUV increase is associated with an increase in the height of the model exobase and an enhanced planetary ion production, leading to, e.g., enhanced massloading of the solar wind flow.

Fig. 3 illustrates the escaping planetary O⁺ and C⁺ ions from Mars in the global hybrid simulation. In all the runs, a notable asymmetry of planetary ions in the xz -plane between the $z > 0$ and $z < 0$ hemispheres is seen due to the solar wind pickup of heavy ions, whereas as the xy -plane (dawn-dusk plane) is symmetric due to the zero upstream flow-aligned IMF component B_x (Jarvinen & Kallio, 2014). In the 1 EUV_☉ run, the planetary ions follow the morphology of the nominal Mars-solar wind interaction: there is the pickup ion plume along the convection electric field E_{sw} and the tailward escape in the wake (Kallio et al., 2010; Dong et al., 2017). In the 3 and 10 EUV_☉ runs, the system becomes heavily massloaded and the interaction appears more comet-like, with a dense ion cloud at low altitudes and pickup and tailward escape at higher altitudes, compared to the nominal run.

6.1. Escape Rates

Table 4 summarizes the production, impact and escape rates of the planetary ions obtained from the hybrid simulations for the three different EUV cases.

Since the initial energy of newly born hot ions is higher than those of newly born cold ions, the former start with larger gyroradii and can therefore escape more easily than the cold ions with small gyroradii. This effect is most distinct for the 1 EUV_⊙ case, while for 10 EUV_⊙, also most of the cold ions already have sufficient initial energies in order to escape.

The ratio of escape rate to the production rate of planetary ions increases with increasing EUV in the global hybrid simulation runs. This results from the expansion of the neutral profiles with higher EUV conditions. When higher planetary neutral densities, and, thus, higher planetary ion production, occur at higher altitudes, less of those ions find their way back near the planet for precipitation. In other words, for higher EUV fluxes the planetary ions massload the solar wind at a higher rate relative to the production rate, as suggested in earlier studies (Chaufray et al., 2007). This is especially clear for the cold population, whereas hot populations are quite extended already for the 1 EUV_⊙ case and most of the produced hot ions escape in all runs. An extreme example of the higher massloading rate is the cold O⁺ impact rates, which decrease from 3 EUV_⊙ to 10 EUV_⊙ (Martinez et al., 2019).

For present Mars (1 EUV_⊙), the total O⁺ and C⁺ escape rates are found to be $\sim 1.05 \cdot 10^{25} \text{ s}^{-1}$ and $\sim 1.9 \cdot 10^{23} \text{ s}^{-1}$, respectively, (see Table 4). Our total O⁺ escape rate for 1 EUV_⊙ is slightly lower but agrees well with the O⁺ escape rate obtained by Jarvinen et al. (2018) of $1.7 \times 10^{25} \text{ s}^{-1}$. Jarvinen et al. (2018) studied the O⁺ energization through the interaction between the solar wind and the Martian exosphere with the above described global hybrid model. These authors compared their results with magnetic field and particle observations of Mars Express and MAVEN missions and were able to reproduce the observed large-scale structures of the induced magnetosphere as well as the Martian plasma environment and heavy ion plume, as seen by the multi-spacecraft observations. Therefore, our O⁺ ion escape and impact rates for present Mars are well within the constraints of in situ spacecraft observations.

It should also be noted that the obtained O⁺ escape rate is of the same order of magnitude than the observed heavy ion escape rates from Mars during solar

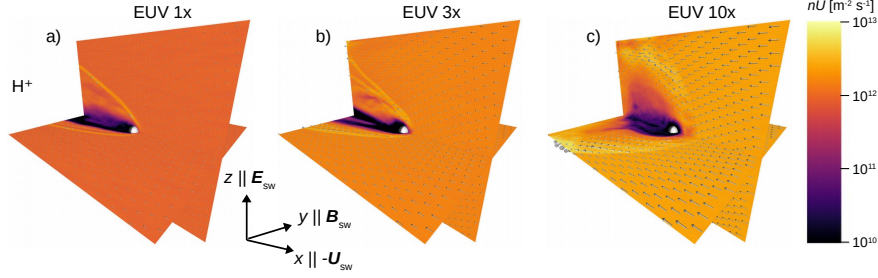


Figure 2: An overview of the Martian induced magnetosphere in the three global hybrid simulation runs. The coloring on the xy ($z = 0$) and xz ($y = 0$) planes gives the solar wind proton bulk number flux. Grey vectors show the morphology of the solar wind bulk flow and the vectors have the same scaling in each panel. Black arrows show the orientation of the coordinate axes and upstream undisturbed solar wind convection electric field (\vec{E}_{sw}), IMF (\vec{B}_{sw}) and bulk velocity (\vec{U}_{sw}) vectors.

maximum conditions (Lundin et al., 1990; Ramstad et al., 2013). However, it is closer to the O^+ escape rate for a quiet Sun than for an active Sun in the study by Fang et al. (2013), and only slightly higher than the retrieved O^+ loss rates of Chassefière & Leblanc (2004), Chassefière & Leblanc (2011), and Dong et al. (2018) (see also Fig. 4). For C^+ , our escape rates are slightly below the values of Chassefière & Leblanc (2004), and Chassefière & Leblanc (2011). All in all, our ion escape rates in the nominal case are well within the same order of magnitude than in previous studies.

For the 3 EUV_{\odot} case, the vast majority of the cold ions have energies of a few eV (with an average of ~ 1.1 and ~ 0.9 eV for O^+ and C^+ , respectively), while the hot ions have energies up to some tens of keV (with an average of ~ 10 and ~ 20 keV for hot O^+ and hot C^+ , respectively); the energy distributions of the precipitating planetary O^+ and C^+ ions at the lower boundary for all 3 EUV cases can be found in the supplement. The total O^+ ion escape rate of $\sim 6.6 \cdot 10^{26} \text{ s}^{-1}$ is about three times higher than the corresponding photochemical escape rate of $\sim 2.1 \cdot 10^{26} \text{ s}^{-1}$, as obtained in Amerstorfer et al. (2017). The total C^+ escape rate of $\sim 2 \cdot 10^{26} \text{ s}^{-1}$ are more than 3 times higher than those of the suprathermal C atoms (Amerstorfer et al., 2017) at that time. According

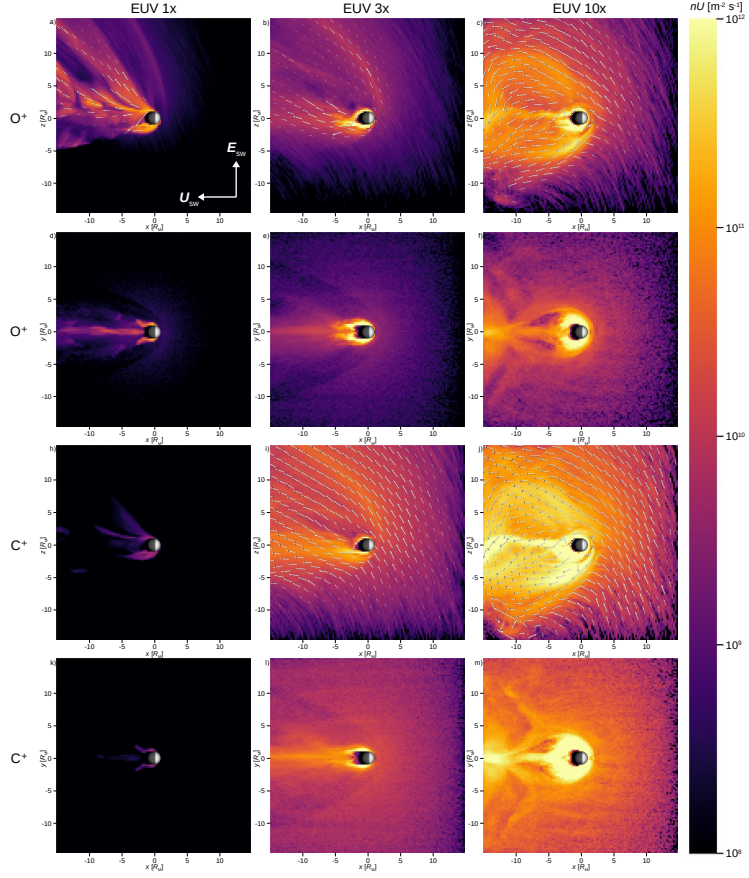


Figure 3: Planetary ions in the three global hybrid simulation runs. The coloring on the xz ($y = 0$) and xy ($z = 0$) planes gives the bulk number flux. Grey vectors show the morphology of the planetary ion bulk flow per species and the vectors have the same scaling in each panel. Two top rows are the O^+ ions and the two bottom rows are the C^+ ions.

to our simulations and in agreement with the results presented in Dong et al. (2018), ion escape becomes the dominant loss process at Mars when its atmosphere is exposed to fluxes $\geq 3 \text{ EUV}_{\odot}$. The main reason for this enhanced ion escape is related to the expansion of the upper atmosphere, which results in a larger planetary cross section for the incoming solar wind plasma and a larger ionization rate. Suprathermal atoms produced e.g. by dissociative recombination have to move through a denser background atmosphere from their main production region to the extended exobase level, leading to the hot particles colliding more often and thus being more easily thermalized, which results in a lower total escape rate. At present, the distance between the main production region of suprathermal atoms and the exobase level are close to each other so that many hot atoms with energies higher than the escape energy can reach the exobase. Therefore, escape of suprathermal atoms is the dominant non-thermal atmospheric escape process for heavy particles on present Mars.

For 10 EUV_{\odot} , our total escape rate of O^+ ions reaches $\sim 1.2 \times 10^{27} \text{ s}^{-1}$, which is also in good agreement with the value obtained by Dong et al. (2018) of $\sim 1.1 \times 10^{27} \text{ s}^{-1}$. These authors, however, did not model the CO_2 -related C^+ escape rates. As illustrated in Fig. 1, the majority of the CO_2 molecules are dissociated in the 10 EUV_{\odot} case with C atoms dominating the exosphere, resulting in a C^+ escape rate of $\sim 4.7 \times 10^{27} \text{ s}^{-1}$ according to our global hybrid model. Since C atoms originate from CO_2 molecules, this can also be seen as the escape rate of CO_2 at $\sim 3.8 \text{ Ga}$. Here, the corresponding oxygen can be lost to space or oxidized onto the surface (Lammer et al., 2003).

In comparison to Boesswetter et al. (2010), who also modeled the escape of O^+ and CO_2^+ over the last 4.5 Ga by means of a 3D hybrid model, our loss rates and those of Dong et al. (2018) for 10 EUV_{\odot} are significantly lower. The reason for this discrepancy is their use of upper atmosphere profiles corresponding to present atmospheric CO_2 mixing ratios, which results in much higher IR-cooling and less expansion, while our profiles and those of Dong et al. (2018) are based on more accurate thermosphere models. In addition, the solar wind velocities and densities used by Boesswetter et al. (2010) are significantly higher but outdated.

The same atmospheric profiles as in Boesswetter et al. (2010) (i.e. assuming no dissociation of the CO₂ molecules) were also used by Terada et al. (2009) and Sakata et al. (2020) and are therefore not accurate (Tian et al., 2009; Scherf & Lammer, 2021).

Table 4: O⁺ and C⁺ production, impact and escape rates, and the production ratios in the three analysed EUV cases.

EUV level	Species	Production rate [1/s]	Impact rate [1/s]	Escape rate [1/s]	Escape/Production ratio
1	Cold O ⁺	$1.64 \cdot 10^{25}$	$7.61 \cdot 10^{24}$	$8.78 \cdot 10^{24}$	0.54
	Hot O ⁺	$1.68 \cdot 10^{24}$	$4.14 \cdot 10^{22}$	$1.63 \cdot 10^{24}$	0.98
	Total O ⁺			$1.04 \cdot 10^{25}$	
	Cold C ⁺	$2.84 \cdot 10^{23}$	$1.24 \cdot 10^{23}$	$1.60 \cdot 10^{23}$	0.56
	Hot C ⁺	$3.23 \cdot 10^{22}$	$6.83 \cdot 10^{20}$	$3.16 \cdot 10^{22}$	0.98
	Total C ⁺			$1.90 \cdot 10^{23}$	
3	Cold O ⁺	$7.68 \cdot 10^{26}$	$1.17 \cdot 10^{26}$	$6.50 \cdot 10^{26}$	0.85
	Hot O ⁺	$1.44 \cdot 10^{25}$	$2.06 \cdot 10^{23}$	$1.42 \cdot 10^{25}$	0.99
	Total O ⁺			$6.64 \cdot 10^{26}$	
	Cold C ⁺	$1.12 \cdot 10^{26}$	$1.51 \cdot 10^{25}$	$9.70 \cdot 10^{25}$	0.87
	Hot C ⁺	$1.01 \cdot 10^{26}$	$6.08 \cdot 10^{23}$	$1.00 \cdot 10^{26}$	0.99
	Total C ⁺			$1.97 \cdot 10^{26}$	
10	Cold O ⁺	$1.06 \cdot 10^{27}$	$4.17 \cdot 10^{25}$	$1.02 \cdot 10^{27}$	0.96
	Hot O ⁺	$1.75 \cdot 10^{26}$	$1.61 \cdot 10^{24}$	$1.73 \cdot 10^{26}$	0.99
	Total O ⁺			$1.2 \cdot 10^{27}$	
	Cold C ⁺	$4.04 \cdot 10^{27}$	$1.13 \cdot 10^{26}$	$3.92 \cdot 10^{27}$	0.97
	Hot C ⁺	$7.94 \cdot 10^{26}$	$3.77 \cdot 10^{24}$	$7.90 \cdot 10^{26}$	1.00
	Total C ⁺			$4.70 \cdot 10^{27}$	

By using the impact rates of exospheric O⁺ and C⁺ ions we also calculate the corresponding sputter escape rates for O, CO₂, CO, C, ³⁶Ar, and ³⁸Ar. Table 5 shows the escape rates of these elements for the 1, 3, and 10 EUV_☉ cases; the calculated yields and the various parameters used for obtaining the sputter rates can be found in the supplement material.

Table 5: Sputter escape rates in the three analysed EUV cases for O, CO₂, CO, C, ³⁶Ar and ³⁸Ar.

EUV level	Incident Ion	O	CO ₂	CO	C	Ar ³⁶	Ar ³⁸
1	Cold O	$8.7 \cdot 10^{24}$	$1.0 \cdot 10^{24}$	$4.3 \cdot 10^{23}$	$4.5 \cdot 10^{21}$	$1.8 \cdot 10^{20}$	$2.8 \cdot 10^{19}$
	Cold C	$1.3 \cdot 10^{23}$	$5.1 \cdot 10^{23}$	$6.0 \cdot 10^{21}$	$6.8 \cdot 10^{19}$	$2.5 \cdot 10^{18}$	$4.0 \cdot 10^{17}$
	Hot O	$7.4 \cdot 10^{22}$	$7.3 \cdot 10^{21}$	$4.1 \cdot 10^{21}$	$3.7 \cdot 10^{19}$	$1.8 \cdot 10^{18}$	$2.8 \cdot 10^{17}$
	Hot C	$8.7 \cdot 10^{20}$	$7.9 \cdot 10^{19}$	$4.6 \cdot 10^{19}$	$4.4 \cdot 10^{17}$	$2.0 \cdot 10^{16}$	$3.1 \cdot 10^{15}$
	Total	$8.9 \cdot 10^{24}$	$1.5 \cdot 10^{24}$	$4.4 \cdot 10^{23}$	$4.6 \cdot 10^{21}$	$1.8 \cdot 10^{20}$	$2.9 \cdot 10^{19}$
3	Cold O	$6.6 \cdot 10^{25}$	$4.3 \cdot 10^{22}$	$8.1 \cdot 10^{23}$	$6.5 \cdot 10^{23}$	$1.6 \cdot 10^{20}$	$1.9 \cdot 10^{19}$
	Cold C	$5.3 \cdot 10^{24}$	$3.4 \cdot 10^{21}$	$6.4 \cdot 10^{22}$	$5.6 \cdot 10^{22}$	$1.3 \cdot 10^{19}$	$1.6 \cdot 10^{18}$
	Hot O	$3.9 \cdot 10^{23}$	$1.3 \cdot 10^{21}$	$9.5 \cdot 10^{21}$	$3.1 \cdot 10^{21}$	$3.2 \cdot 10^{18}$	$4.2 \cdot 10^{17}$
	Hot C	$1.0 \cdot 10^{24}$	$3.9 \cdot 10^{21}$	$2.7 \cdot 10^{22}$	$8.0 \cdot 10^{21}$	$9.4 \cdot 10^{18}$	$1.2 \cdot 10^{18}$
	Total	$7.3 \cdot 10^{25}$	$5.1 \cdot 10^{22}$	$9.1 \cdot 10^{23}$	$7.1 \cdot 10^{23}$	$1.8 \cdot 10^{20}$	$2.2 \cdot 10^{19}$
10	Cold O	$3.0 \cdot 10^{25}$	$7.6 \cdot 10^{20}$	$1.5 \cdot 10^{23}$	$7.1 \cdot 10^{24}$	$1.4 \cdot 10^{20}$	$1.5 \cdot 10^{19}$
	Cold C	$5.5 \cdot 10^{25}$	$1.6 \cdot 10^{21}$	$3.1 \cdot 10^{23}$	$1.2 \cdot 10^{25}$	$3.2 \cdot 10^{20}$	$3.4 \cdot 10^{19}$
	Hot O	$2.6 \cdot 10^{24}$	$1.3 \cdot 10^{20}$	$2.0 \cdot 10^{22}$	$4.9 \cdot 10^{23}$	$2.2 \cdot 10^{19}$	$2.4 \cdot 10^{18}$
	Hot C	$4.8 \cdot 10^{24}$	$2.7 \cdot 10^{20}$	$3.7 \cdot 10^{22}$	$9.1 \cdot 10^{23}$	$4.4 \cdot 10^{19}$	$4.8 \cdot 10^{18}$
	Total	$9.2 \cdot 10^{25}$	$2.8 \cdot 10^{21}$	$5.1 \cdot 10^{23}$	$2.0 \cdot 10^{25}$	$5.2 \cdot 10^{20}$	$5.6 \cdot 10^{19}$

Figures 4 and 5 summarize our simulation outcomes for O (Fig. 4) and C (Fig. 5), ion escape (panels b) and sputtering (panels c) together with the results for suprathermal escape from Amerstorfer et al. (2017) (panels a) for all three EUV cases. The figure includes loss rates of several other earlier studies, i.e. hot oxygen loss through dissociative recombination (DR), ion escape and sputtering by Chassefière & Leblanc (2004) and Chassefière & Leblanc (2011), ion escape and sputtering by Fang et al. (2013), ion escape and suprathermal escape by Dong et al. (2018), sputtering for present-day based on MAVEN measurements (Leblanc et al., 2018), and extrapolations for the loss of hot oxygen through DR by Cravens et al. (2017) and Lillis et al. (2017). It is obvious, however, that extrapolations to higher EUV fluxes as applied by Lillis et al. (2017) through a simple power law fit can hardly yield appropriate escape rates, since the production of suprathermal atoms does not exponentially increase with increasing EUV flux, as outlined above and discussed in detail in Amerstorfer

et al. (2017).

For sputtering, our theoretical result for C at present Mars are by about an order of magnitude lower as recently inferred by Leblanc et al. (2018) and as those compiled by Chassefière & Leblanc (2004) and Chassefière & Leblanc (2011). However, if we add-up the sputter escape rates of all C species, i.e., CO₂, CO, and C, then we obtain similar escape rates as Leblanc et al. (2018) for all C species together. In our case, much less CO₂ is dissociated into C, thereby leading to lower C but higher CO₂ sputter rates.

Our oxygen sputter escape rates for 1 EUV_☉ ($8.9 \times 10^{24} \text{ s}^{-1}$), on the other hand, are significantly higher than those ($4 \times 10^{23} \text{ s}^{-1}$) estimated by Leblanc et al. (2018) and also higher than those ($2 \times 10^{24} \text{ s}^{-1}$) given by Wang et al. (2014, 2015). As noted by Leblanc et al. (2018), they would have found an escape rate of $1 \times 10^{24} \text{ s}^{-1}$ if they had used a precipitation rate of $\approx 1 \times 6.5 \times 10^{24} \text{ O}^+/\text{s}^{-1}$ and the analytical relation between precipitating flux and induced atmospheric escape of Wang et al. (2015). The actual lower value of Leblanc et al. (2018) is attributed to the additional energy absorption of N and N₂, which was not considered by Wang et al. (2015). Since we also neglect N and N₂ in our calculations, it is more reasonable to compare our oxygen sputter rates with those of Wang et al. (2014, 2015), showing that our rates are 4-5 times higher. The main reason for this difference seems to be due to the fact that the analytical model results in higher yields for oxygen (Johnson, 1994; Johnson et al., 2000) than the model of Wang et al. (2015).

Our retrieved total escape rates of O for higher EUV fluxes fit quite well with the results of Chassefière & Leblanc (2011), and Dong et al. (2018). In all these cases, ion escape becomes the dominant process for increased EUV fluxes. For C, our ion escape rates are about 1000 times higher than those of Chassefière & Leblanc (2004) and Chassefière & Leblanc (2011). The reason for this is simple, though. In our case, at 10 EUV almost all of the CO₂ is dissociated leading to strong escape of carbon atoms due to their lighter weight and the accompanying expansion of the upper atmosphere, which is itself related to the dissociation of the infrared-cooler CO₂. Due to this effect, Mars could have lost a significant

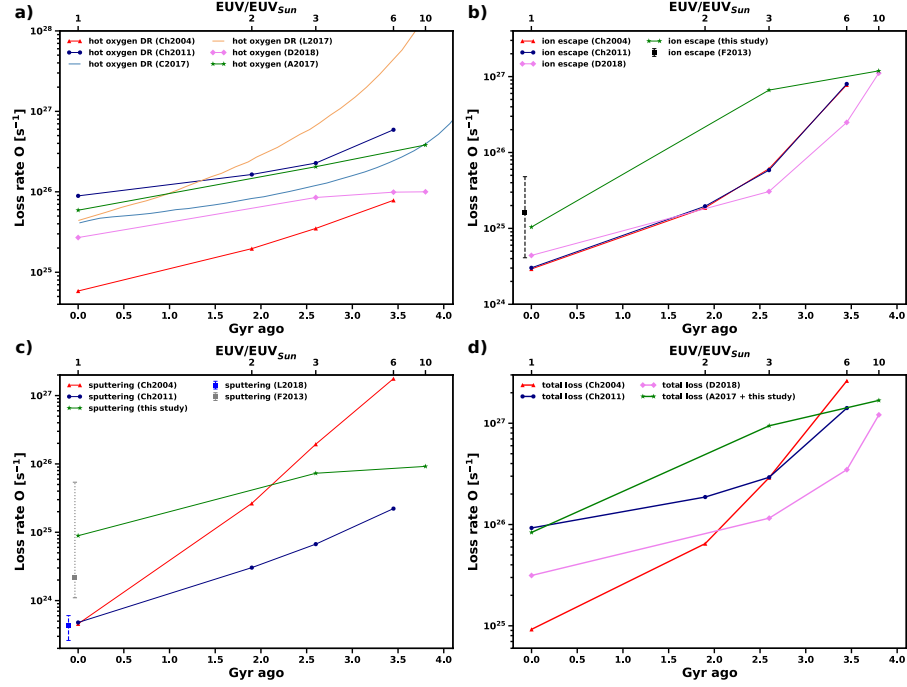


Figure 4: Oxygen escape rates (a) dissociative escape; b) ion escape; c) sputtering; d) total escape of a-c) from our present and previous work A2017 (Amerstorfer et al., 2017) compared with several other studies. Here, Ch2004 refers to Chassefière & Leblanc (2004), Ch2011 to Chassefière & Leblanc (2011), C2016 to Cravens et al. (2017), L2017 to Lillis et al. (2017), F2013 to Fang et al. (2013), D2018 to (Dong et al., 2018), L2018 to Leblanc et al. (2018). The abbreviation DR stands for dissociative recombination.

amount of CO_2 over its history.

Finally, it has to be noted that the integrated loss to space over time might be even higher than retrieved from our simulation, since we have chosen quiet conditions for the solar flux as well as for the solar wind, thereby not taking into account extreme solar events such as flares and interplanetary coronal mass ejections. Even though these extreme events only play a minor role for atmospheric escape at Mars at present-day, they likely have been significantly more frequent in the distant past (e.g., Airapetian et al., 2016; Odert et al., 2017; Kay et al., 2019).

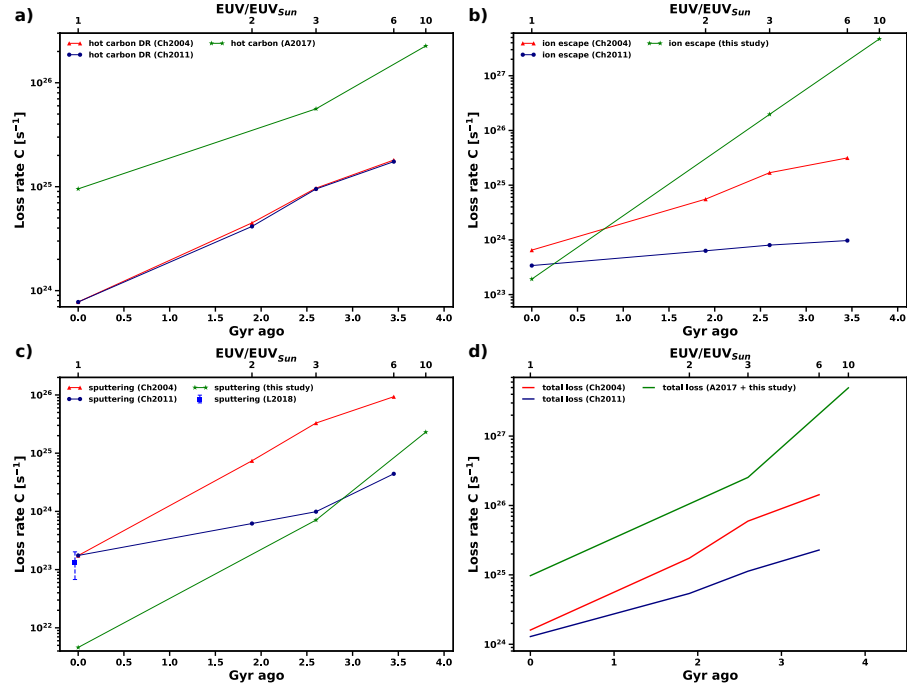


Figure 5: Carbon escape rates (a) suprathermal; b) ion escape; c) sputtering; d) total escape of a-c) from our present and previous work A2017 (Amerstorfer et al., 2017) compared with several other studies. Here, Ch2004 refers to Chassefière & Leblanc (2004), Ch2011 to Chassefière & Leblanc (2011), L2018 to Leblanc et al. (2018). The abbreviation DR stands for dissociative recombination.

6.2. Atmospheric Evolution

Figure 6 shows the integrated CO₂ surface partial pressure evolution from today until 4.1 Ga, caused by the three main non-thermal atmospheric escape processes, namely suprathermal escape (Amerstorfer et al., 2017), as well as sputtering and ion escape as modeled in the present work. It is seen that sputtering induced escape does not contribute significantly to the total loss of CO₂, which is clearly dominated by ion escape for flux values ≥ 3 EUV_⊙. Earlier than 4.1 Ga, the situation is getting more complex due to thermal escape becoming significant (e.g. Tian et al., 2009) and the presence of an intrinsic Martian magnetic field, which vanished around this time in the past (e.g. Lillis et al., 2013). While it is yet not entirely clear, how such an intrinsic magnetic field might affect the efficiency of non-thermal escape processes (being it a funnel or a shield, e.g. Gunell et al., 2018; Blackman & Tarduno, 2018; Egan et al., 2019; Scherf & Lammer, 2021), it does not affect thermal escape, which could have been as high as $\sim 10^{30} \text{ s}^{-1}$ for carbon at ~ 4.5 Ga (Tian et al., 2009). It also has to be noted that this surface pressure evolution does only include losses to space through thermal and non-thermal escape; carbonate formation as additional sinks could in principle allow for even higher pressures, since the total reservoir of CO₂ in carbonates at Mars is estimated to be up to ≈ 1 bar (e.g. Jakosky, 2019). Similarly, atmospheric erosion through asteroid impacts could have provided another sink (e.g. Pham & Karatekin, 2016). All of these sinks together, however, only provide a theoretical maximum pressure at a certain time that could have been lost until the present-day. The real pressure could have been significantly lower at any point in time (see, e.g., Scherf & Lammer, 2021, for a discussion on this issue).

To fit suprathermal, ion, and sputtering escape rates in between the three different EUV values, for each escape process a separate exponential function in the form of

$$[\text{CO}_2]_{\text{esc}}(t) = [\text{CO}_2]_{\text{esc}_0} e^{bt}, \quad (34)$$

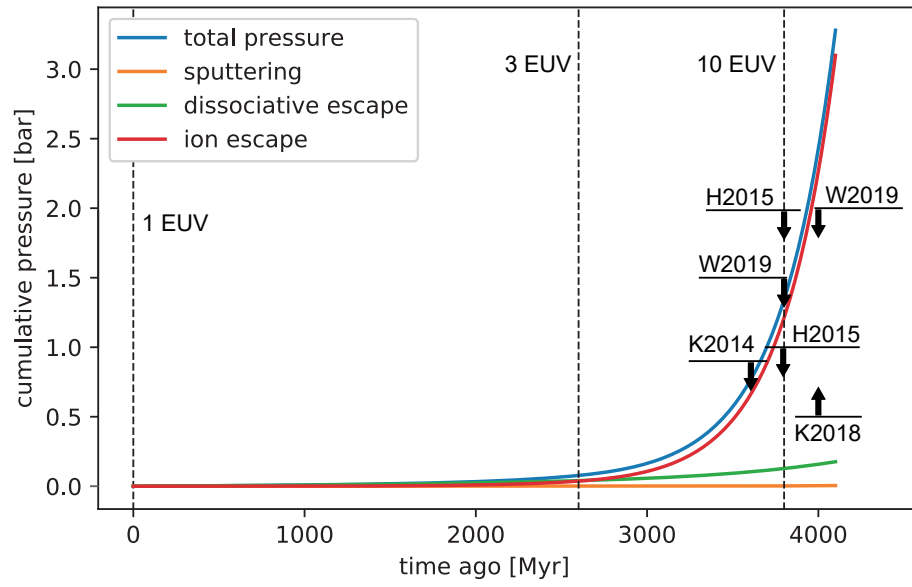


Figure 6: Modeled CO₂-related surface pressure evolution from present to 4.1 Ga caused by various atmospheric escape processes. The dissociative escape rate have been taken from Amerstorfer et al. (2017), while ion escape and sputtering correspond to the results of this study. Here, K2014 refers to Kite et al. (2014), H2015 to Hu et al. (2015), K2018 to Kurokawa et al. (2018), and W2019 to Warren et al. (2019).

was used (Chassefière & Leblanc, 2011). For the periods between 1 – 3 and 3 – 10 EUV_⊙, the factor b is determined by inserting $t = 2.6$ and $t = 3.8$ Ga, respectively, into Equation (34), while for $t > 3.8$ Ga, the escape was kept constant at the value of 10 EUV_⊙. This might be an underestimation, however, since the EUV flux should have been higher prior to 3.8 Ga leading also to higher non-thermal escape.

From Figure 6 it can be seen that more than 3 bar of CO₂ could have been theoretically removed through the combination of the different atmospheric escape processes over the last 4.1 Ga. Moreover, the partial surface pressure of CO₂ of ≤ 0.8 bar at about 3.6 Ga is in agreement with the upper atmospheric surface pressure of 0.9 ± 0.1 bar as estimated from the size distribution of ancient craters by Kite et al. (2014).

From current atmospheric $^{13}\text{C}/^{12}\text{C}$, rock and soil carbonate measurements, Hu et al. (2015) constrained the atmospheric surface pressure of Mars at ~ 3.8 Ga to < 1 bar. Only scenarios with large amounts of carbonate deposition in open-water systems would permit higher values of up to 1.8 bar (Hu et al., 2015). According to our results, a maximum of ~ 1.4 bar could have been left in the atmosphere at 3.8 Ga, which is within the upper range of Hu et al. (2015).

Our result is also in agreement with another recent study by Jakosky (2019) which estimated the CO₂ inventory on Mars including its loss to space over time based on various previously published models. By reconstructing the Martian present-day $^{13}\text{C}/^{12}\text{C}$ ratio of $\delta^{13}\text{C} \approx 45\text{‰}$ (Mahaffy et al., 2013; Webster et al., 2013) from an assumed initial value of -20 to -30‰ based on carbon measurements within Martian meteorites (Wright et al., 1986), and by also taking into account the formation of carbonates which preferentially removes the heavier isotope from the atmosphere, Jakosky (2019) found a lower limit of escape to space of about 1–2 bar CO₂ from 4.3 Ga until present. This is well below our maximum loss of ≈ 3 bar from 4.1 Ga, which indicates that our result might also be in agreement with the evolution of the Martian $^{13}\text{C}/^{12}\text{C}$ ratio over time. However, simulating the evolution of $^{13}\text{C}/^{12}\text{C}$ within our model would have been beyond the scope of this study, since other factors such as the formation

of carbonates can also significantly alter the isotopic ratio of carbon.

Any change in the $^{36}\text{Ar}/^{38}\text{Ar}$ ratio, on the other hand, is predominantly shaped by escape to space and replenishment through volcanic outgassing. For its evolution and the therewith connected atmospheric escape over time, we compare the CO_2 sputter escape rates of Slipski & Jakosky (2016) with our calculations. Figure 7a shows that, if one takes the argon escape rates by Slipski & Jakosky (2016), sputtering would have been able to create the present day $^{36}\text{Ar}/^{38}\text{Ar}$ value from its initial ratio as preserved within ALH 84001 for an initial pressure range at 4.1 Ga of 0.7 – 1.3 bar, if one does not alter the sputtering efficiency, i.e. $s_f = 1$ in equation (30). For the maximum of 1.3 bar, no argon should have been supplied by volcanic outgassing into the atmosphere since the cessation of the Martian dynamo, therefore all of the atmospheric Ar must have been accumulated before then due to the required vanishing volcanic outgassing factor. Kurokawa et al. (2018) suggested that the volcanic gases contain only a negligible amount of noble gases. Therefore, pressures towards the maximum would be in agreement with them. For pressures above 1.3 bar, sputtering of Ar isotopes based on the values of Slipski & Jakosky (2016) is not efficient enough to remove the required amount during the time span of 4.1 billion years, whereas for pressures below 0.7 bar sputtering becomes so efficient that no amount of outgassing is able to provide enough ^{36}Ar to reach the preserved ratio of the 4.1 Ga old Mars meteorite ALH 84001. For lower or higher pressures, one would have to change the value of s_f .

Figure 7b shows the same, but with argon sputter values that are derived from our CO_2 sputtering via Equation 30. As can be seen, if keeping $s_f = 1$ (green line), no initial pressure can reproduce the present-day $^{36}\text{Ar}/^{38}\text{Ar}$ ratio which might be an indication that our rates are too high (please also note that the green line reaches a minimum at around 600 million years ago (Ma); at this time almost no ^{36}Ar is left in the atmosphere and ongoing ^{38}Ar sputtering together with outgassing of ^{36}Ar leads to an increase of the ratio towards the present). If one sets $s_f = 0.08 - 0.13$, however, one can reproduce

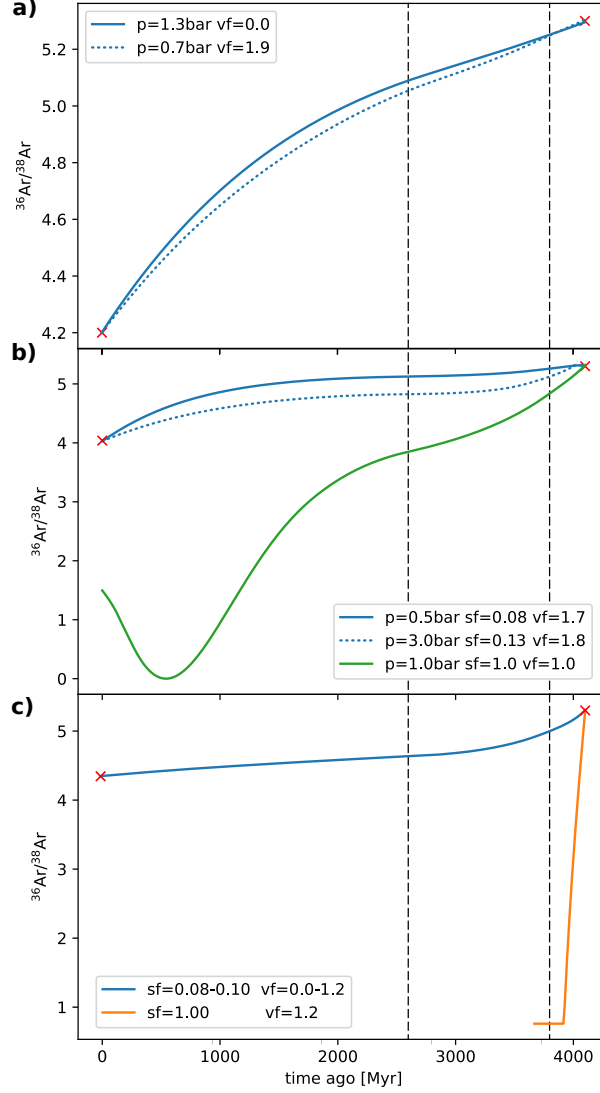


Figure 7: Reproduction attempts from Mars' ALH 84001 based initial $^{36}\text{Ar}/^{38}\text{Ar}$ ratio ~ 4.1 Ga to the present atmospheric value with various initial CO_2 -related surface pressure values and volcanic outgassing factors v_f . Panel a) is derived with argon sputtering values for $s_f = 1$ taken from Slipski & Jakosky (2016), panel b) with the values derived from CO_2 sputtering as retrieved from our simulations. If one sets $s_f = 1$ no solution can be found, whereas the $^{36}\text{Ar}/^{38}\text{Ar}$ ratio can be reproduced for $s_f = 0.16$ for pressures between 1 and 2.7 bar. Panel c) is derived directly from our Ar sputtering values as given in Table 5. The present-day ratio can only be reproduced if we reduce our sputter rates to $s_f = 0.16 - 0.18$, indicating that the total sputtering likely was lower than in our simulation. In this case no minimum and maximum CO_2 pressures can be derived.

today's $^{36}\text{Ar}/^{38}\text{Ar}$ ratio for 0.5–3.0 bar which is, although partially overlapping, significantly broader than the pressure range that we retrieved with the values of Slipski & Jakosky (2016). However, as pointed out by Zahnle et al. (2008), such a thick CO_2 -dominated atmosphere might not have been photochemically stable on early Mars but was likely converted to a CO-dominated atmosphere through the dissociation of CO_2 into CO and O.

Figure 7c illustrates the evolution of the $^{36}\text{Ar}/^{38}\text{Ar}$ ratio by taking our derived argon sputter rates through calculated via Equation 20 as shown in Table 5. In this case, no minimum and maximum CO_2 pressure can be derived since Ar sputtering is not directly scaled with the evolution of CO_2 . Moreover, the present-day ratio of $^{36}\text{Ar}/^{38}\text{Ar}$ can, again, only be reproduced if we reduce our sputter ratios to a narrow range of $s_f = 0.08 - 0.10$. This indicates that the maximum sputtering escape that we retrieve from our simulation is too high. If we assume $s_f = 1.0$, all atmospheric ^{36}Ar will escape after a short period of time, as can be clearly seen in Figure 7c (orange line). For values of $s_f < 0.08$, on the other hand, the fractionation would be too weak. If we apply the same tight range of sputter efficiency, $s_f = 0.08 - 0.10$, and outgassing scaling factor, $v_f = 0.0 - 1.2$ that works for our directly calculated Ar sputter values (Fig. 7c) to the method applied in Fig. 7b, i.e., deriving argon sputtering from our CO_2 sputtering, we receive a very restricted pressure range for 4.1 Ga of only 1.2–1.4 bar.

The overestimation of the sputter escape rates can have several reasons. A main reason might be that the surface pressure of the Martian atmosphere was significantly below our maximum value of up to 3 bar during the Noachian eon. If there would have been less atmosphere to escape, there would have also been less planetward-scattered ions to drive sputtering escape, thereby also reducing the fractionation between ^{36}Ar and ^{38}Ar , which also points to the results illustrated in Figures 7a and b, and to the various studies on the Noachian CO_2 partial pressure values discussed above (Hu et al., 2015; Kite et al., 2014; Kurokawa et al., 2018). We, moreover, did not include ^{40}Ar , the product from the radioactive decay of ^{40}K , into our sputter calculations which might have

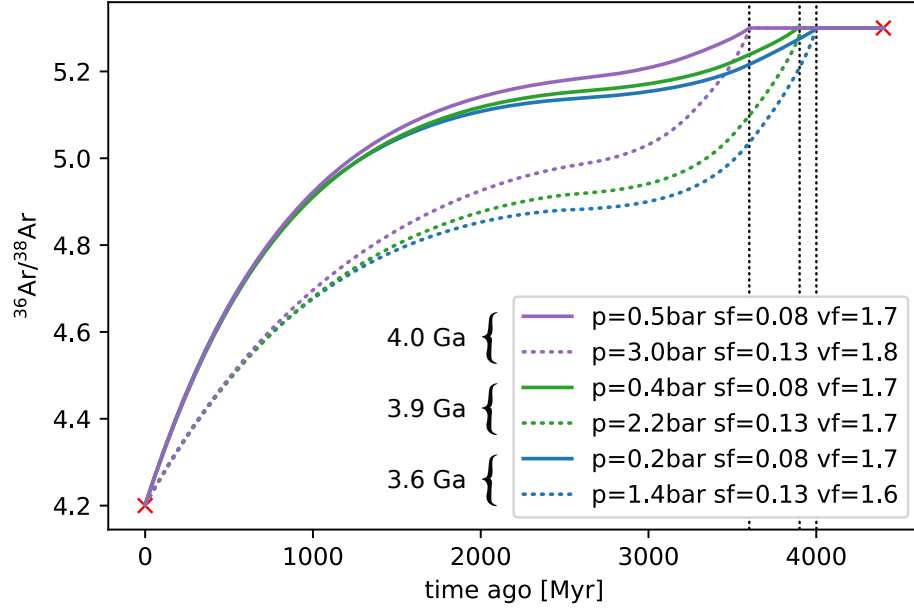


Figure 8: The evolution of the $^{36}\text{Ar}/^{38}\text{Ar}$ ratio as for case (b) of Fig. 7 but for different initial starting points of fractionation with our derived sputtering values. If fractionation started later, lower pressures are needed for reproducing $^{36}\text{Ar}/^{38}\text{Ar}$.

reduced the sputter rates of ^{36}Ar and ^{38}Ar , since some of the precipitating ions could have also sputtered ^{40}Ar instead of one of the other isotopes. For including ^{40}Ar into the simulation one has to implement the whole radioactive K-Ar system into the model, which is beyond the scope of our present study; however, we are planning to include this in our future work since it might be a crucial factor for reconstructing the evolution of $^{36}\text{Ar}/^{38}\text{Ar}$. Moreover, one should also note that especially for these extended early atmospheres another reason for some overestimation of the Argon isotope sputtering rates may result from the analytical model approach. For finding and minimizing potential inherent errors in our calculation, future studies might, therefore, apply a combined upper atmosphere solar wind interaction Monte Carlo sputtering model to compare its outcome with the analytical approach that we have chosen in our study.

Another reason for the overestimation, however, could be the cessation of the intrinsic Martian magnetic field. The measured value of $^{36}\text{Ar}/^{38}\text{Ar}$ in the

meteorite ALH84001 only shows that at ~ 4.1 Ga the argon isotope fractionation was 5.3. It does not indicate that sputtering immediately started to fractionate ^{36}Ar from ^{38}Ar . If the intrinsic magnetic field of Mars ceased later than at 4.1 Ga, fractionation would have also started later, which could also be a possible scenario, since Lillis et al. (2013) found a time of cessation of 4.0-4.1 Ga and Milbury et al. (2012) reported a later cessation time of even ~ 3.6 Ga. If fractionation through sputtering started later, the present-day $^{36}\text{Ar}/^{38}\text{Ar}$ ratio can be reproduced with a pressure even below 0.5 bar at 4.1 Ga.

Figure 8 shows the initial pressure for different earlier starting points of fractionation. If fractionation started at 3.9 Ga, the initial pressure for $s_f = 0.08 - 0.13$ at this particular time would have been between 0.4–2.2 bar, and for 3.6 Ga 0.2–1.4 bar. For $s_f = 0.08 - 0.10$ and $v_f = 0.0 - 1.2$, the pressure range reduces to 0.8-1.0 bar for 3.9 Ga, and 0.5-0.6 bar for 3.6 Ga, respectively.

Another possibility of a delayed on-set of Ar fractionation could be that Mars built up a CO_2 atmosphere only later than 4.1 Ga with no dense atmosphere before. This might indeed be an additional option, since thermal escape is expected to have been very strong early-on during the pre-Noachian eon (Tian et al., 2009), leading to the potential escape of any early Martian CO_2 -dominated atmosphere (Scherf & Lammer, 2021), while argon might have been too heavy to escape thermally. Both, outgassing (e.g. Grott et al., 2011) and impact delivery (e.g. Pham & Karatekin, 2016) could have led to the built-up of at least a few hundred mbars of CO_2 after 4.1 Ga.

Keeping this in mind, it seems possible that the Martian atmosphere at 4.1 Ga was towards the lower range of potential pressure values that could reproduce $^{36}\text{Ar}/^{38}\text{Ar}$, i.e. 0.5 – 3 bar CO_2 for $s_f = 0.08 - 0.13$, or even below with fractionation starting later-on. In such a case, it is unlikely that early Mars had been a warm and wet planet, but might have been cold and dry with some transient events of liquid water triggered by impacts or volcanic outgassing.

7. Conclusion

We simulated the ion escape of CO₂ related dissociation products C and O over the Martian history back until ~ 4.1 Ga, the probably earliest time of the cessation of the Martian internal magnetic dynamo. The escape of cold and hot O⁺ and C⁺ was simulated for 1 EUV_⊙ (today), 3 EUV_⊙ (~ 2.6 Ga), and 10 EUV_⊙ (~ 3.8 Ga) with a 3D global hybrid upper atmosphere model (Kallio & Janhunen, 2003; Dyadechkin et al., 2013), using the atmospheric profiles of Tian et al. (2009) and the hot O and C profiles of (Amerstorfer et al., 2017). We further investigated atmospheric sputtering of O, CO₂, CO, C, ³⁶Ar and ³⁸Ar caused by precipitating O⁺ and C⁺ ions calculated from our 3D hybrid simulations. We found that ion escape becomes the dominant loss process for solar fluxes ≥ 3 EUV_⊙ with loss rates at 10 EUV_⊙ of $\sim 1.1 \times 10^{27} \text{ s}^{-1}$ for O⁺ and $\sim 4.7 \times 10^{27} \text{ s}^{-1}$ for C⁺. For the same EUV flux, sputtering yields much lower escape rates of about $9.2 \times 10^{25} \text{ s}^{-1}$ for O and $2.4 \times 10^{25} \text{ s}^{-1}$ for C. If one extrapolates the total escape of CO₂ back in time until 4.1 Ga by assuming that any lost C atom originates from a CO₂ molecule, we find a maximum cumulative total CO₂ partial pressure of more than 3 bar. Escape to space can, therefore, be considered being able to have removed enough CO₂ to explain the loss of a potential early thick Martian atmosphere from the Noachian eon until the present.

Moreover, we also studied the fractionation of argon isotopes from its initial chondritic value of $^{36}\text{Ar}/^{38}\text{Ar} \sim 5.3$ at 4.1 Ga through sputtering and volcanic outgassing until the present day. We found that only CO₂ pressures with $\leq 0.5\text{--}3.0\text{ bar}$ at 4.1 Ga can reproduce the present day value, if argon fractionation by sputtering indeed started at 4.1 Ga, the time when the magnetic dynamo of Mars is believed to have faded away. Whether Mars could have had such a dense atmosphere at this time, however, is a matter of debate, since strong thermal escape prior to ~ 4.0 Ga (Tian et al., 2009) might have prevented the built-up of such a dense early atmosphere.

However, the present-day ratio of $^{36}\text{Ar}/^{38}\text{Ar}$ could also be reproduced if

Mars outgassed a CO₂-dominated atmosphere with ≤ 1 bar later than 4.1 Ga and/or if fractionation of argon through sputtering started < 4 Ga. In this case, the required partial pressure needs to be $\leq 0.4 - 2.2$ bar, while even later at 3.6 Ga it would have only been $\leq 0.2 - 1.4$ bar. In case Mars had only a tenuous CO₂-dominated atmosphere during the pre-Noachian and only a few 100 mbar during the Noachian, it likely was a cold and dry body with only transient events of surficial liquid water. Therefore, further investigations based on isotopic fractionation, atmospheric escape, but also atmosphere-surface interactions, are needed in order to better constrain the climate conditions of early Mars and the subsequent evolution of its atmosphere. This not only includes a simultaneous reconstruction of $^{13}\text{C}/^{12}\text{C}$ over time together with $^{36}\text{Ar}/^{38}\text{Ar}$ by taking into account the diverse processes that can affect both isotopic ratios, but, ultimately, also to explain the evolution of other volatile species at Mars besides CO₂ and Ar, such as H₂O and N within one comprehensive model.

8. Acknowledgements

HIML, HL, and UVA acknowledge support by the Austrian Science Fundation via the project P 24247-N16. HL and SD acknowledge support by the Austrian Science Fund (FWF) NFN project S11601-N16, “Pathways to Habitability: From Disks to Active Stars, Planets and Life” and the related FWF NFN subproject S11607-N16 “Particle/Radiative Interactions with Upper Atmospheres of Planetary Bodies under Extreme Stellar Conditions”. The work of RJ and EK was supported by the Academy of Finland (Decision No. 310444). Figures 2 and 3 were created using the VisIt open-source visualisation tool (Childs et al., 2012). We acknowledge Feng Tian from the Macau University of Technology and Science for giving support to this work.

References

- Airapetian, V. S., Gloer, A., Gronoff, G., Hébrard, E., & Danchi, W. (2016). Prebiotic chemistry and atmospheric warming of early Earth by an active

- young Sun. *Nature Geoscience*, *9*, 452–455. doi:10.1038/ngeo2719.
- Amerstorfer, U. V., Gröller, H., Lichtenegger, H., Lammer, H., Tian, F., Noack, L., Scherf, M., Johnstone, C., Tu, L., & Güdel, M. (2017). Escape and evolution of Mars’s CO₂ atmosphere: Influence of suprathermal atoms. *J. Geophys. Res.*, *122*, 1321–1337. doi:10.1002/2016JE005175.
- Atreya, S. K., Trainer, M. G., Franz, H. B., Wong, M. H., Manning, H. L. K., Malespin, C. A., Mahaffy, P. R., Conrad, P. G., Brunner, A. E., Leshin, L. A., Jones, J. H., Webster, C. R., Owen, T. C., Pepin, R. O., & Navarro-González, R. (2013). Primordial argon isotope fractionation in the atmosphere of Mars measured by the SAM instrument on Curiosity and implications for atmospheric loss. *Geophys. Res. Lett.*, *40*, 5605–5609. doi:10.1002/2013GL057763.
- Avicé, G., & Marty, B. (2020). Perspectives on Atmospheric Evolution from Noble Gas and Nitrogen Isotopes on Earth, Mars & Venus. *Space Sci. Rev.*, *216*, 36. doi:10.1007/s11214-020-00655-0. arXiv:2003.11431.
- Bauer, S. J., & Lammer, H. (2004). *Planetary aeronomy : atmosphere environments in planetary systems*. Physics of Earth and Space Environments. Springer-Verlag Berlin Heidelberg.
- Blackman, E. G., & Tarduno, J. A. (2018). Mass, energy, and momentum capture from stellar winds by magnetized and unmagnetized planets: implications for atmospheric erosion and habitability. *MNRAS*, *481*, 5146–5155. doi:10.1093/mnras/sty2640. arXiv:1801.00895.
- Boesswetter, A., Lammer, H., Kulikov, Y., Motschmann, U., & Simon, S. (2010). Non-thermal water loss of the early Mars: 3D multi-ion hybrid simulations. *Planet. Space Sci.*, *58*, 2031–2043. doi:10.1016/j.pss.2010.10.003.
- Bougher, S. W., Pawlowski, D., Bell, J. M., Nelli, S., McDunn, T., Murphy, J. R., Chizek, M., & Ridley, A. (2015). Mars Global Ionosphere-Thermosphere Model: Solar cycle, seasonal, and diurnal variations of the

- Mars upper atmosphere. *Journal of Geophysical Research (Planets)*, *120*, 311–342. doi:10.1002/2014JE004715.
- Chassefière, E., & Leblanc, F. (2004). Mars atmospheric escape and evolution; interaction with the solar wind. *Planet. Space Sci.*, *52*, 1039–1058. doi:10.1016/j.pss.2004.07.002.
- Chassefière, E., & Leblanc, F. (2011). Methane release and the carbon cycle on Mars. *Planet. Space Sci.*, *59*, 207–217. doi:10.1016/j.pss.2010.09.004.
- Chaufray, J. Y., Modolo, R., Leblanc, F., Chanteur, G., Johnson, R. E., & Luhmann, J. G. (2007). Mars solar wind interaction: Formation of the Martian corona and atmospheric loss to space. *Journal of Geophysical Research (Planets)*, *112*, E09009. doi:10.1029/2007JE002915.
- Cravens, T. E., Rahmati, A., Fox, J. L., Lillis, R., Bougher, S., Luhmann, J., Sakai, S., Deighan, J., Lee, Y., Combi, M., & Jakosky, B. (2017). Hot oxygen escape from Mars: Simple scaling with solar EUV irradiance. *Journal of Geophysical Research (Space Physics)*, *122*, 1102–1116. doi:10.1002/2016JA023461.
- Curdt, W., Brekke, P., Feldman, U., Wilhelm, K., Dwivedi, B. N., Schühle, U., & Lemaire, P. (2001). The SUMER spectral atlas of solar-disk features. *Astron. Astrophys.*, *375*, 591–613. doi:10.1051/0004-6361:20010364.
- Curdt, W., Landi, E., & Feldman, U. (2004). The SUMER spectral atlas of solar coronal features. *Astron. Astrophys.*, *427*, 1045–1054. doi:10.1051/0004-6361:20041278.
- de Pater, I., & Lissauer, J. J. (2015). *Planetary Sciences*. (2nd ed.). Cambridge University Press.
- di Achille, G., & Hynek, B. M. (2010). Ancient ocean on Mars supported by global distribution of deltas and valleys. *Nature Geoscience*, *3*, 459–463. doi:10.1038/ngeo891.

- Dong, C., Bougher, S. W., Ma, Y., Toth, G., Nagy, A. F., & Najib, D. (2014). Solar wind interaction with Mars upper atmosphere: Results from the one-way coupling between the multifluid MHD model and the MTGCM model. *Geophys. Res. Lett.*, *41*, 2708–2715. doi:10.1002/2014GL059515.
- Dong, C., Lee, Y., Ma, Y., Lingam, M., Bougher, S., Luhmann, J., Curry, S., Toth, G., Nagy, A., Tennishev, V., Fang, X., Mitchell, D., Brain, D., & Jakosky, B. (2018). Modeling Martian Atmospheric Losses over Time: Implications for Exoplanetary Climate Evolution and Habitability. *ApJ*, *859*, L14. doi:10.3847/2041-8213/aac489. arXiv:1805.05016.
- Dong, Y., Fang, X., Brain, D. A., McFadden, J. P., Halekas, J. S., Connerney, J. E. P., Eparvier, F., Andersson, L., Mitchell, D., & Jakosky, B. M. (2017). Seasonal variability of Martian ion escape through the plume and tail from MAVEN observations. *Journal of Geophysical Research (Space Physics)*, *122*, 4009–4022. doi:10.1002/2016JA023517.
- Dyadechkin, S., Kallio, E., & Jarvinen, R. (2013). A new 3-D spherical hybrid model for solar wind interaction studies. *J. Geophys. Res.*, *118*, 5157–5168. doi:10.1002/jgra.50497.
- Egan, H., Jarvinen, R., Ma, Y., & Brain, D. (2019). Planetary magnetic field control of ion escape from weakly magnetized planets. *MNRAS*, *488*, 2108–2120. doi:10.1093/mnras/stz1819. arXiv:1907.02978.
- Fang, X., Bougher, S. W., Johnson, R. E., Luhmann, J. G., Ma, Y., Wang, Y.-C., & Liemohn, M. W. (2013). The importance of pickup oxygen ion precipitation to the mars upper atmosphere under extreme solar wind conditions. *Geophysical Research Letters*, *40*, 1922–1927. doi:10.1002/grl.50415.
- Fang, X., Bougher, S. W., Johnson, R. E., Luhmann, J. G., Ma, Y., Wang, Y.-C., & Liemohn, M. W. (2013). The importance of pickup oxygen ion precipitation to the Mars upper atmosphere under extreme solar wind conditions. *Geophys. Res. Lett.*, *40*, 1922–1927. doi:10.1002/grl.50415.

- Fox, J. L., & Hać, A. (1997). The $^{15}\text{N}/^{14}\text{N}$ isotope fractionation in dissociative recombination of N_2^+ . *J. Geophys. Res.*, *102*, 9191–9204. doi:10.1029/97JE00086.
- G. Luhmann, J., & Kozyra, J. (1991). Dayside pickup oxygen ion precipitation at venus and mars: Spatial distributions, energy deposition and consequences. *JGR*, *96*, 5457–5467. doi:10.1029/90JA01753.
- Greeley, R., & Schneid, B. D. (1991). Magma Generation on Mars: Amounts, Rates, and Comparisons with Earth, Moon, and Venus. *Science*, *254*, 996–998. doi:10.1126/science.254.5034.996.
- Gröller, H., Lammer, H., Lichtenegger, H. I. M., Pfleger, M., Dutuit, O., Shematovich, V. I., Kulikov, Y. N., & Biernat, H. K. (2012). Hot oxygen atoms in the Venus nightside exosphere. *Geophys. Res. Lett.*, *39*. doi:10.1029/2011GL050421.
- Gröller, H., Lichtenegger, H., Lammer, H., & Shematovich, V. I. (2014). Hot oxygen and carbon escape from the martian atmosphere. *Planet. Space Sci.*, *98*, 93–105. doi:10.1016/j.pss.2014.01.007.
- Gröller, H., Shematovich, V. I., Lichtenegger, H. I. M., Lammer, H., Pfleger, M., Kulikov, Y. N., Macher, W., Amerstorfer, U. V., & Biernat, H. K. (2010). Venus’ atomic hot oxygen environment. *J. Geophys. Res.*, *115*. doi:10.1029/2010JE003697.
- Grott, M., Baratoux, D., Hauber, E., Sautter, V., Mustard, J., Gasnault, O., Ruff, S. W., Karato, S. I., Debaille, V., Knapmeyer, M., Sohl, F., Van Hoolst, T., Breuer, D., Morschhauser, A., & Toplis, M. J. (2013). Long-Term Evolution of the Martian Crust-Mantle System. *Space Sci. Rev.*, *174*, 49–111. doi:10.1007/s11214-012-9948-3.
- Grott, M., Morschhauser, A., Breuer, D., & Hauber, E. (2011). Volcanic outgassing of CO_2 and H_2O on Mars. *Earth and Planetary Science Letters*, *308*, 391–400. doi:10.1016/j.epsl.2011.06.014.

- Gunell, H., Maggiolo, R., Nilsson, H., Stenberg Wieser, G., Slapak, R., Lindkvist, J., Hamrin, M., & De Keyser, J. (2018). Why an intrinsic magnetic field does not protect a planet against atmospheric escape. *A&A*, *614*, L3. doi:10.1051/0004-6361/201832934.
- Hu, R., Kass, D. M., Ehlmann, B. L., & Yung, Y. L. (2015). Tracing the fate of carbon and the atmospheric evolution of Mars. *Nature Communications*, *6*, 10003. doi:10.1038/ncomms10003. arXiv:1512.00758.
- Huebner, W. F., & Carpenter, C. W. (1979). *Solar Photo Rate Coefficients*. Scientific Report LA-8085-MS Los Alamos.
- Huebner, W. F., Keady, J. J., & Lyon, S. P. (1992). Solar photo rates for planetary atmospheres and atmospheric pollutants. *Astrophys. Space Sci.*, *195*, 1–289. doi:10.1007/BF00644558.
- Huebner, W. F., & Mukherjee, J. (2015). Photoionization and photodissociation rates in solar and blackbody radiation fields. *Planet. Space Sci.*, *106*, 11–45. doi:10.1016/j.pss.2014.11.022.
- Hurowitz, J. A., Grotzinger, J. P., Fischer, W. W., McLennan, S. M., Milliken, R. E., Stein, N., Vasavada, A. R., Blake, D. F., Dehouck, E., Eigenbrode, J. L., Fairén, A. G., Frydenvang, J., Gellert, R., Grant, J. A., Gupta, S., Herkenhoff, K. E., Ming, D. W., Rampe, E. B., Schmidt, M. E., Siebach, K. L., Stack-Morgan, K., Sumner, D. Y., & Wiens, R. C. (2017). Redox stratification of an ancient lake in Gale crater, Mars. *Science*, *356*, aah6849. doi:10.1126/science.aah6849.
- Hutchins, K. S., & Jakosky, B. M. (1996). Evolution of Martian atmospheric argon: Implications for sources of volatiles. *J. Geophys. Res.*, *101*, 14933–14950. doi:10.1029/96JE00860.
- Jakosky, B. M. (2019). The CO₂ inventory on Mars. *Planet. Space Sci.*, *175*, 52–59. doi:10.1016/j.pss.2019.06.002.

- Jakosky, B. M., Brain, D., Chaffin, M., Curry, S., Deighan, J., Grebowsky, J., Halekas, J., Leblanc, F., Lillis, R., Luhmann, J. G., Andersson, L., Andre, N., Andrews, D., Baird, D., Baker, D., Bell, J., Benna, M., Bhattacharyya, D., Bougher, S., Bowers, C., Chamberlin, P., Chaufray, J. Y., Clarke, J., Collinson, G., Combi, M., Connerney, J., Connour, K., Correia, J., Crabb, K., Crary, F., Cravens, T., Crismani, M., Delory, G., Dewey, R., DiBraccio, G., Dong, C., Dong, Y., Dunn, P., Egan, H., Elrod, M., England, S., Eparvier, F., Ergun, R., Eriksson, A., Esman, T., Espley, J., Evans, S., Fallows, K., Fang, X., Fillingim, M., Flynn, C., Fogle, A., Fowler, C., Fox, J., Fujimoto, M., Garnier, P., Girazian, Z., Groeller, H., Gruesbeck, J., Hamil, O., Hanley, K. G., Hara, T., Harada, Y., Hermann, J., Holmberg, M., Holsclaw, G., Houston, S., Inui, S., Jain, S., Jolitz, R., Kotova, A., Kuroda, T., Larson, D., Lee, Y., Lee, C., Lefevre, F., Lentz, C., Lo, D., Lugo, R., Ma, Y. J., Mahaffy, P., Marquette, M. L., Matsumoto, Y., Mayyasi, M., Mazelle, C., McClintock, W., McFadden, J., Medvedev, A., Mendillo, M., Meziane, K., Milby, Z., Mitchell, D., Modolo, R., Montmessin, F., Nagy, A., Nakagawa, H., Narvaez, C., Olsen, K., Pawlowski, D. et al. (2018). Loss of the Martian atmosphere to space: Present-day loss rates determined from MAVEN observations and integrated loss through time. *Icarus*, *315*, 146–157. doi:10.1016/j.icarus.2018.05.030.
- Jakosky, B. M., Grebowsky, J. M., Luhmann, J. G., & Brain, D. A. (2015). Initial results from the MAVEN mission to Mars. *Geophys. Res. Lett.*, *42*, 8791–8802. doi:10.1002/2015GL065271.
- Jakosky, B. M., Pepin, R. O., Johnson, R. E., & Fox, J. L. (1994). Mars Atmospheric Loss and Isotopic Fractionation by Solar-Wind-Induced Sputtering and Photochemical Escape. *Icarus*, *111*, 271–288. doi:10.1006/icar.1994.1145.
- Jakosky, B. M., & Phillips, R. J. (2001). Mars’ volatile and climate history. *Nature*, *412*, 237–244.

- Jakosky, B. M., Slipski, M., Benna, M., Mahaffy, P., Elrod, M., Yelle, R., Stone, S., & Alsaed, N. (2017). Mars’ atmospheric history derived from upper-atmosphere measurements of $^{38}\text{Ar}/^{36}\text{Ar}$. *Science*, *355*, 1408–1410. doi:10.1126/science.aai7721.
- Jarvinen, R., Brain, D. A., Modolo, R., Fedorov, A., & Holmström, M. (2018). Oxygen Ion Energization at Mars: Comparison of MAVEN and Mars Express Observations to Global Hybrid Simulation. *Journal of Geophysical Research (Space Physics)*, *123*, 1678–1689. doi:10.1002/2017JA024884.
- Jarvinen, R., & Kallio, E. (2014). Energization of planetary pickup ions in the solar system. *J. Geophys. Res.*, *119*, 219–236. doi:10.1002/2013JE004534.
- Johnson, R. E. (1990). *Energetic charged-particle interactions with atmospheres and surfaces* volume 69 of *Physics and Chemistry in Space*. Springer-Verlag.
- Johnson, R. E. (1994). Plasma-induced sputtering of an atmosphere. *Space Sci. Rev.*, *69*, 215–253.
- Johnson, R. E., Schnellenberger, D., & Wong, M. C. (2000). The sputtering of an oxygen thermosphere by energetic O^+ . *J. Geophys. Res.*, *105*, 1659–1670. doi:10.1029/1999JE001058.
- Johnstone, C. P., Güdel, M., Brott, I., & Lüftinger, T. (2015a). Stellar winds on the main-sequence. II. The evolution of rotation and winds. *A&A*, *577*, A28. doi:10.1051/0004-6361/201425301. arXiv:1503.07494.
- Johnstone, C. P., Güdel, M., Lüftinger, T., Toth, G., & Brott, I. (2015b). Stellar winds on the main-sequence. I. Wind model. *A&A*, *577*, A27. doi:10.1051/0004-6361/201425300. arXiv:1503.06669.
- Kallio, E., & Janhunen, P. (2003). Modelling the solar wind interaction with Mercury by a quasineutral hybrid model. *Ann. Geophys.*, *21*, 2133–2145.
- Kallio, E., Liu, K., Jarvinen, R., Pohjola, V., & Janhunen, P. (2010). Oxygen ion escape at Mars in a hybrid model: High energy and low energy ions. *Icarus*, *206*, 152–163. doi:10.1016/j.icarus.2009.05.015.

- Kay, C., Airapetian, V. S., Lüftinger, T., & Kochukhov, O. (2019). Frequency of Coronal Mass Ejection Impacts with Early Terrestrial Planets and Exoplanets around Active Solar-like Stars. *ApJ*, *886*, L37. doi:10.3847/2041-8213/ab551f. [arXiv:1911.02701](#).
- Kite, E. S., Williams, J.-P., Lucas, A., & Aharonson, O. (2014). Low palaeo-pressure of the martian atmosphere estimated from the size distribution of ancient craters. *Nature Geoscience*, *7*, 335–339. doi:10.1038/ngeo2137. [arXiv:1304.4043](#).
- Kurokawa, H., Kurosawa, K., & Usui, T. (2018). A lower limit of atmospheric pressure on early Mars inferred from nitrogen and argon isotopic compositions. *Icarus*, *299*, 443–459. doi:10.1016/j.icarus.2017.08.020. [arXiv:1708.03956](#).
- Lammer, H., Chassefière, E., Karatekin, Ö., Morschhauser, A., Niles, P. B., Mousis, O., Odert, P., Möstl, U. V., Breuer, D., Dehant, V., Grott, M., Gröller, H., Hauber, E., & Pham, L. B. S. (2013). Outgassing History and Escape of the Martian Atmosphere and Water Inventory. *Space Sci. Rev.*, *174*, 113–154. doi:10.1007/s11214-012-9943-8. [arXiv:1506.06569](#).
- Lammer, H., Leitzinger, M., Scherf, M., Odert, P., Burger, C., Kubyshkina, D., Johnstone, C., Maindl, T., Schäfer, C. M., Güdel, M., Tosi, N., Nikolaou, A., Marcq, E., Erkaev, N. V., Noack, L., Kislyakova, K. G., Fossati, L., Pilat-Lohinger, E., Ragossnig, F., & Dorfi, E. A. (2020a). Constraining the early evolution of Venus and Earth through atmospheric Ar, Ne isotope and bulk K/U ratios. *Icarus*, *339*, 113551. doi:10.1016/j.icarus.2019.113551.
- Lammer, H., Lichtenegger, H. I. M., Kolb, C., Ribas, I., Guinan, E. F., Abart, R., & Bauer, S. J. (2003). Loss of water from Mars: Implications for the oxidation of the soil. *Icarus*, *165*, 9–25. doi:10.1016/S0019-1035(03)00170-2.
- Lammer, H., Scherf, M., Kurokawa, H., Ueno, Y., Burger, C., Maindl, T., Johnstone, C., Leitzinger, M., Benedikt, M., Fossati, L., Kislyakova, K. G.,

- Marty, B., Avice, G., Fegley, B., & Odert, P. (2020b). Loss and fractionation of noble gas isotopes and moderately volatile elements from planetary embryos and early venus, earth and mars. *Space Sci. Rev.*, *submitted*.
- Lammer, H., Zerkle, A. L., Gebauer, S., Tosi, N., Noack, L., Scherf, M., Pilat-Lohinger, E., Güdel, M., Grenfell, J. L., Godolt, M., & Nikolaou, A. (2018). Origin and evolution of the atmospheres of early Venus, Earth and Mars. *A&A Rev.*, *26*, 2. doi:10.1007/s00159-018-0108-y.
- Lapen, T. J., Richter, M., Brandon, A. D., Debaille, V., Beard, B. L., Shafer, J. T., & Peslier, A. H. (2010). A Younger Age for ALH84001 and Its Geochemical Link to Shergottite Sources in Mars. *Science*, *328*, 347. doi:10.1126/science.1185395.
- Leblanc, F., Chassefière, E., Gillmann, C., & Breuer, D. (2012). Mars' atmospheric ^{40}Ar : A tracer for past crustal erosion. *Icarus*, *218*, 561–570. doi:10.1016/j.icarus.2012.01.006.
- Leblanc, F., Martinez, A., Chaufray, J. Y., Modolo, R., Hara, T., Luhmann, J., Lillis, R., Curry, S., McFadden, J., Halekas, J., & Jakosky, B. (2018). On Mars's Atmospheric Sputtering After MAVEN's First Martian Year of Measurements. *Geophys. Res. Lett.*, *45*, 4685–4691. doi:10.1002/2018GL077199.
- Lillis, R. J., Deighan, J., Fox, J. L., Bougher, S. W., Lee, Y., Combi, M. R., Cravens, T. E., Rahmati, A., Mahaffy, P. R., Benna, M., Elrod, M. K., McFadden, J. P., Ergun, R. E., Andersson, L., Fowler, C. M., Jakosky, B. M., Thiemann, E., Eparvier, F., Halekas, J. S., Leblanc, F., & Chaufray, J.-Y. (2017). Photochemical escape of oxygen from Mars: First results from MAVEN in situ data. *Journal of Geophysical Research (Space Physics)*, *122*, 3815–3836. doi:10.1002/2016JA023525.
- Lillis, R. J., Robbins, S., Manga, M., Halekas, J. S., & Frey, H. V. (2013). Time history of the Martian dynamo from crater magnetic field analysis. *Journal of Geophysical Research (Planets)*, *118*, 1488–1511. doi:10.1002/jgre.20105.

- Luhmann, J. G., Johnson, R. E., & Zhang, M. H. G. (1992). Evolutionary impact of sputtering of the martian atmosphere by o^+ pickup ions. *Geophysical Research Letters*, *19*, 2151–2154. doi:10.1029/92GL02485.
- Mahaffy, P. R., Webster, C. R., Atreya, S. K., Franz, H., Wong, M., Conrad, P. G., Harpold, D., Jones, J. J., Leshin, L. A., Manning, H., Owen, T., Pepin, R. O., Squyres, S., Trainer, M., Kemppinen, O., Bridges, N., Johnson, J. R., Minitti, M., Cremers, D., Bell, J. F., Edgar, L., Farmer, J., Godber, A., Wadhwa, M., Wellington, D., McEwan, I., Newman, C., Richardson, M., Charpentier, A., Peret, L., King, P., Blank, J., Weigle, G., Schmidt, M., Li, S., Milliken, R., Robertson, K., Sun, V., Baker, M., Edwards, C., Ehlmann, B., Farley, K., Griffes, J., Grotzinger, J., Miller, H., Newcombe, M., Pilorget, C., Rice, M., Siebach, K., Stack, K., Stolper, E., Brunet, C., Hipkin, V., Léveillé, R., Marchand, G., Sánchez, P. S., Favot, L., Cody, G., Steele, A., Flückiger, L., Lees, D., Nefian, A., Martin, M., Gailhanou, M., Westall, F., Israël, G., Agard, C., Baroukh, J., Donny, C., Gaboriaud, A., Guillemot, P., Lafaille, V., Lorigny, E., Paillet, A., Pérez, R., Saccoccio, M., Yana, C., Armiens-Aparicio, C., Rodríguez, J. C., Blázquez, I. C., Gómez, F. G., Gómez-Elvira, J., Hettrich, S., Malvitte, A. L., Jiménez, M. M., Martínez-Frías, J., Martín-Soler, J., Martín-Torres, F. J., Jurado, A. M., Mora-Sotomayor, L., Caro, G. M., López, S. N., Peinado-González, V., Pla-García, J., Manfredi, J. A. R., Romeral-Planelló, J. J., Fuentes, S. A. S., Martinez, E. S., Redondo, J. T. et al. (2013). Abundance and Isotopic Composition of Gases in the Martian Atmosphere from the Curiosity Rover. *Science*, *341*, 263–266. doi:10.1126/science.1237966.
- Manning, C. V., McKay, C. P., & Zahnle, K. J. (2006). Thick and thin models of the evolution of carbon dioxide on Mars. *Icarus*, *180*, 38–59. doi:10.1016/j.icarus.2005.08.014.
- Martinez, A., Leblanc, F., Chaufray, J. Y., Modolo, R., Witasse, O., Dong, Y., Hara, T., Halekas, J., Lillis, R., McFadden, J., Eparvier, F., Leclercq, L., Luhmann, J., Curry, S., Titov, D., & Jakosky, B. (2019). Influence of

- Extreme Ultraviolet Irradiance Variations on the Precipitating Ion Flux From MAVEN Observations. *Geophys. Res. Lett.*, *46*, 7761–7768. doi:10.1029/2019GL083595.
- Marty, B. (2012). The origins and concentrations of water, carbon, nitrogen and noble gases on Earth. *Earth and Planetary Science Letters*, *313*, 56–66. doi:10.1016/j.epsl.2011.10.040. arXiv:1405.6336.
- Mathew, K. J., & Marti, K. (2001). Early evolution of Martian volatiles: Nitrogen and noble gas components in ALH84001 and Chassigny. *J. Geophys. Res.*, *106*, 1401–1422. doi:10.1029/2000JE001255.
- Mazor, E., Heymann, D., & Anders, E. (1970). Noble gases in carbonaceous chondrites. *Geochim. Cosmochim. Acta*, *34*, 781–824. doi:10.1016/0016-7037(70)90031-1.
- Milbury, C., Schubert, G., Raymond, C. A., Smrekar, S. E., & Langlais, B. (2012). The history of Mars’ dynamo as revealed by modeling magnetic anomalies near Tyrrhenus Mons and Syrtis Major. *Journal of Geophysical Research (Planets)*, *117*, E10007. doi:10.1029/2012JE004099.
- Mittelholz, A., Johnson, C. L., Feinberg, J. M., Langlais, B., & Phillips, R. J. (2020). Timing of the martian dynamo: New constraints for a core field 4.5 and 3.7 Ga ago. *Science Advances*, *6*, eaba0513. doi:10.1126/sciadv.aba0513.
- Morschhauser, A., Grott, M., & Breuer, D. (2011). Crustal recycling, mantle dehydration, and the thermal evolution of Mars. *Icarus*, *212*, 541–558. doi:10.1016/j.icarus.2010.12.028.
- Najib, D., Nagy, A. F., Tóth, G., & Ma, Y. (2011). Three-dimensional, multi-fluid, high spatial resolution MHD model studies of the solar wind interaction with Mars. *Journal of Geophysical Research (Space Physics)*, *116*, A05204. doi:10.1029/2010JA016272.

- Odert, P., Leitzinger, M., Hanslmeier, A., & Lammer, H. (2017). Stellar coronal mass ejections - I. Estimating occurrence frequencies and mass-loss rates. *MNRAS*, *472*, 876–890. doi:10.1093/mnras/stx1969. arXiv:1707.02165.
- Palumbo, A. M., Head, J. W., & Wilson, L. (2020). Rainfall on Noachian Mars: Nature, timing, and influence on geologic processes and climate history. *Icarus*, *347*, 113782. doi:10.1016/j.icarus.2020.113782.
- Pham, L. B. S., & Karatekin, Ö. (2016). Scenarios of atmospheric mass evolution on Mars influenced by asteroid and comet impacts since the late Noachian. *Planet. Space Sci.*, *125*, 1–11. doi:10.1016/j.pss.2015.09.022.
- Sakata, R., Seki, K., Sakai, S., Terada, N., Shinagawa, H., & Tanaka, T. (2020). Effects of an Intrinsic Magnetic Field on Ion Loss From Ancient Mars Based on Multispecies MHD Simulations. *Journal of Geophysical Research (Space Physics)*, *125*, e26945. doi:10.1029/2019JA026945.
- Saxena, P., Killen, R. M., Airapetian, V., Petro, N. E., Curran, N. M., & Mandell, A. M. (2019). Was the Sun a Slow Rotator? Sodium and Potassium Constraints from the Lunar Regolith. *ApJ*, *876*, L16. doi:10.3847/2041-8213/ab18fb. arXiv:1906.05892.
- Scherf, M., & Lammer, H. (2021). Did Mars Possess a Dense Atmosphere During the First ~400 Million Years? *Space Sci. Rev.*, *217*, 2. doi:10.1007/s11214-020-00779-3.
- Sieveka, E. M., & Johnson, R. E. (1984). Ejection of atoms and molecules from Io by plasma-ion impact. *Astrophys. J.*, *287*, 418–426.
- Slipski, M., & Jakosky, B. M. (2016). Argon isotopes as tracers for martian atmospheric loss. *Icarus*, *272*, 212–227. doi:10.1016/j.icarus.2016.02.047.
- Terada, N., Kulikov, Y. N., Lammer, H., Lichtenegger, H. I. M., Tanaka, T., Shinagawa, H., & Zhang, T. (2009). Atmosphere and Water Loss from Early

- Mars Under Extreme Solar Wind and Extreme Ultraviolet Conditions. *Astrobiological*, 9, 55–70. doi:10.1089/ast.2008.0250.
- Tian, F., Kasting, J. F., & Solomon, S. C. (2009). Thermal escape of carbon from the early Martian atmosphere. *Geophys. Res. Lett.*, 36. doi:10.1029/2008GL036513.
- Tu, L., Johnstone, C. P., Güdel, M., & Lammer, H. (2015). The extreme ultraviolet and X-ray Sun in Time: High-energy evolutionary tracks of a solar-like star. *A&A*, 577, L3. doi:10.1051/0004-6361/201526146. [arXiv:1504.04546](#).
- Wallis, M. K. (1989). C, N, O isotope fractionation on Mars: implications for crustal H₂O and SNC meteorites. *Earth and Planetary Science Letters*, 93, 321–324. doi:10.1016/0012-821X(89)90031-9.
- Wang, Y.-C., Luhmann, J. G., Fang, X., Leblanc, F., Johnson, R. E., Ma, Y., & Ip, W.-H. (2015). Statistical studies on Mars atmospheric sputtering by precipitating pickup O⁺: Preparation for the MAVEN mission. *Journal of Geophysical Research (Planets)*, 120, 34–50. doi:10.1002/2014JE004660.
- Wang, Y.-C., Luhmann, J. G., Leblanc, F., Fang, X., Johnson, R. E., Ma, Y., Ip, W.-H., & Li, L. (2014). Modeling of the O⁺ pickup ion sputtering efficiency dependence on solar wind conditions for the Martian atmosphere. *Journal of Geophysical Research (Planets)*, 119, 93–108. doi:10.1002/2013JE004413.
- Warren, A. O., Kite, E. S., Williams, J. P., & Horgan, B. (2019). Through the Thick and Thin: New Constraints on Mars Paleopressure History 3.8 - 4 Ga from Small Exhumed Craters. *Journal of Geophysical Research (Planets)*, 124, 2793–2818. doi:10.1029/2019JE006178.
- Webster, C. R., Mahaffy, P. R., Flesch, G. J., Niles, P. B., Jones, J. H., Leshin, L. A., Atreya, S. K., Stern, J. C., Christensen, L. E., Owen, T., Franz, H., Pepin, R. O., Steele, A., & aff9 (2013). Isotope Ratios of H, C, and O in CO₂

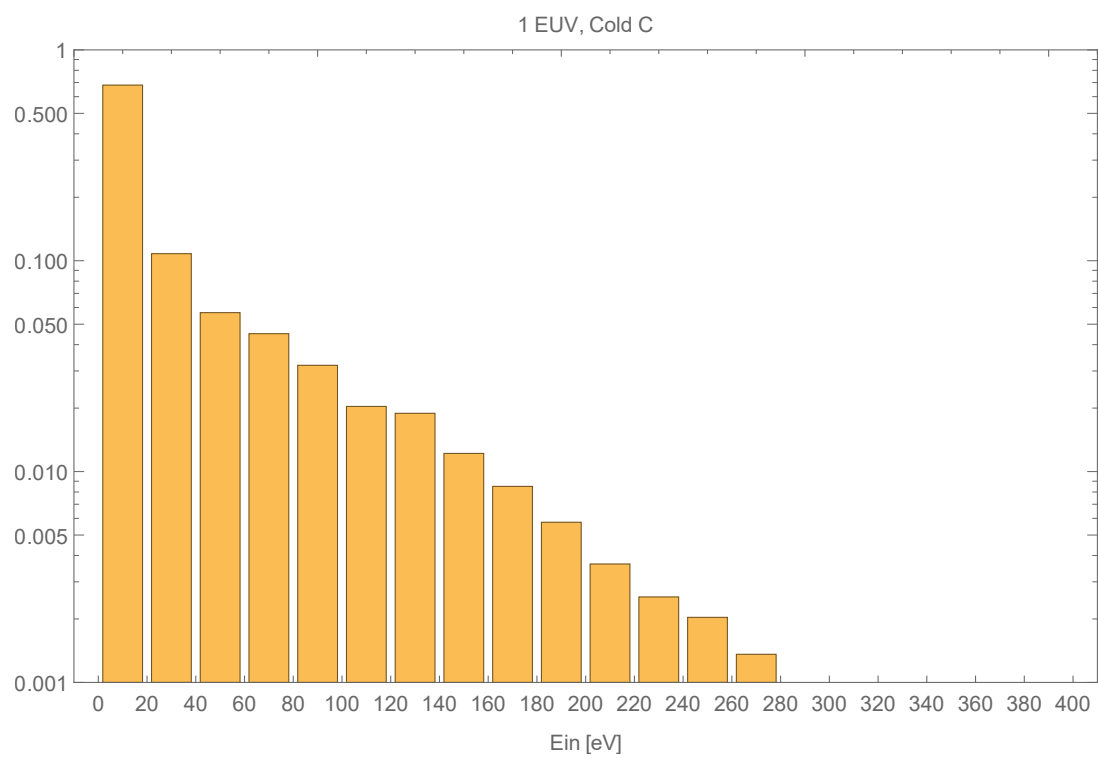
- and H₂O of the Martian Atmosphere. *Science*, *341*, 260–263. doi:10.1126/science.1237961.
- Wright, I. P., Carr, R. H., & Pillinger, C. T. (1986). Carbon abundance and isotopic studies of Shergotty and other shergottite meteorites. *Geochim. Cosmochim. Acta*, *50*, 983–991. doi:10.1016/0016-7037(86)90379-0.
- Zahnle, K., Haberle, R. M., Catling, D. C., & Kasting, J. F. (2008). Photochemical instability of the ancient Martian atmosphere. *Journal of Geophysical Research (Planets)*, *113*, E11004. doi:10.1029/2008JE003160.
- Zahnle, K. J., Gacesa, M., & Catling, D. C. (2019). Strange messenger: A new history of hydrogen on Earth, as told by Xenon. *Geochim. Cosmochim. Acta*, *244*, 56–85. doi:10.1016/j.gca.2018.09.017. arXiv:1809.06960.
- Zhao, J., & Tian, F. (2015). Photochemical escape of oxygen from early Mars. *Icarus*, *250*, 477–481. doi:10.1016/j.icarus.2014.12.032.

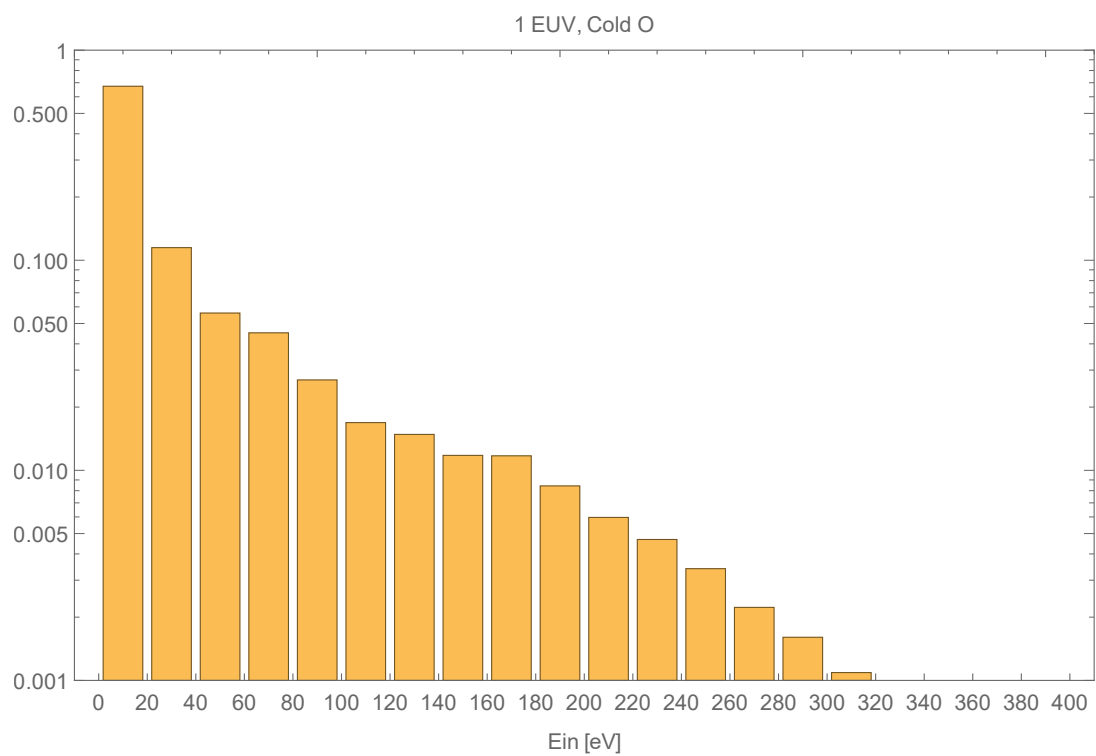
Supplement

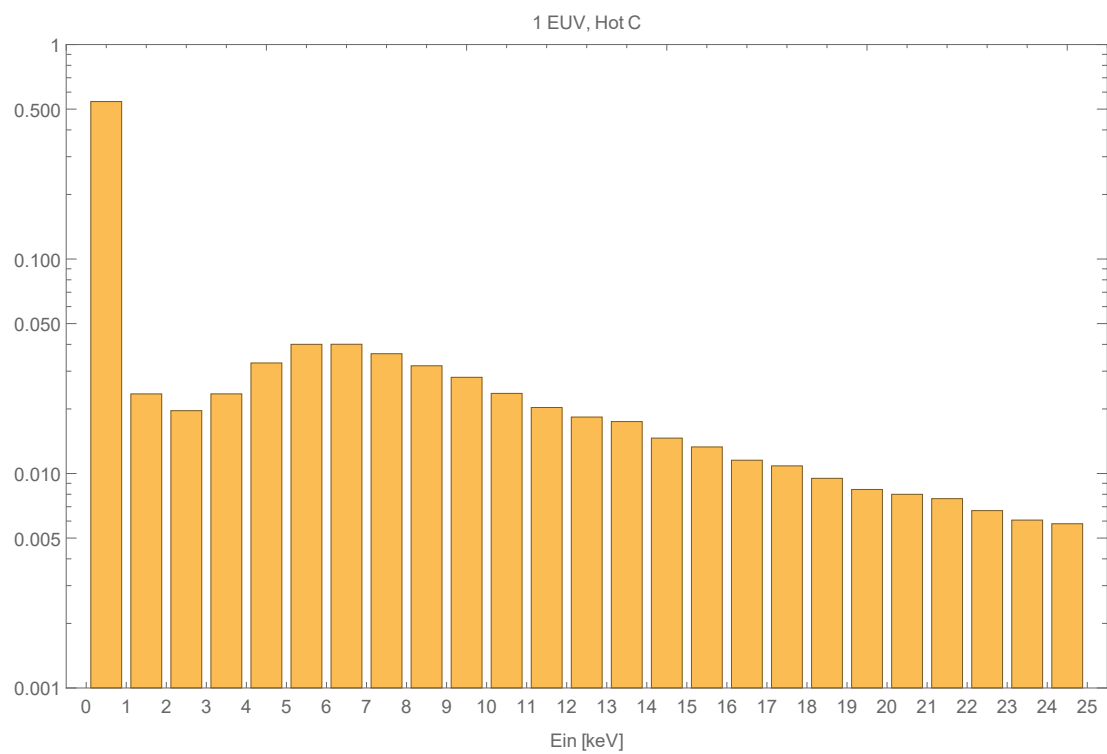
The first 12 figures illustrate the probability distribution of the precipitating O^+ and C^+ ions (cold and hot) that act as sputter agents for the respective lower boundaries of the 1, 3, and 10 EUV cases as a function of energy.

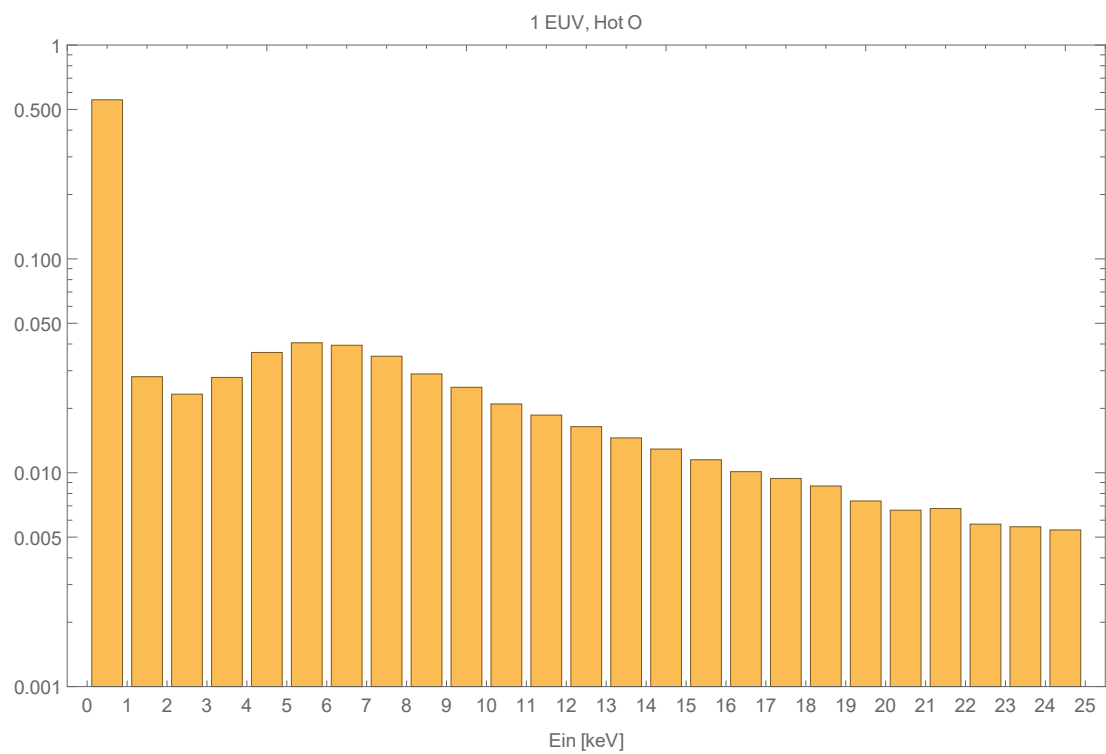
The subsequent 12 tables correspond to the respective sputter parameters and calculated yields for all cases and ions that are needed to calculate sputtering (see Equations in the main article in Section 4).

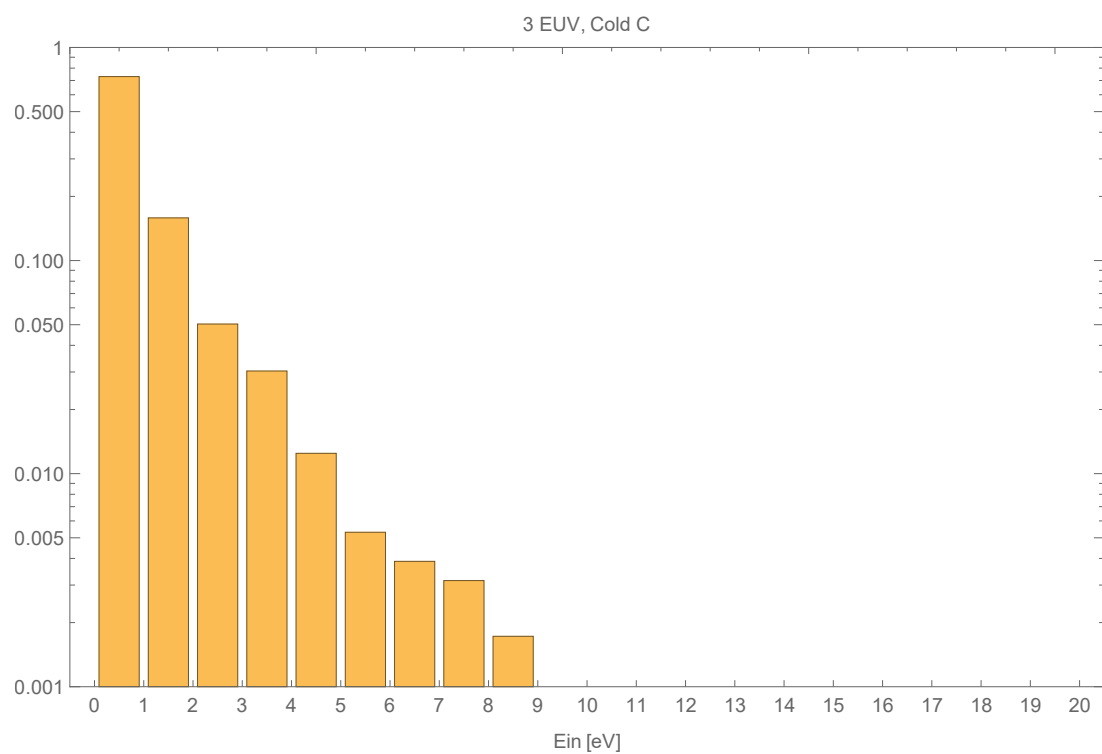
The final 3 tables give the neutral densities of the different species at the respective exobase levels for 1, 3, and 10 EUV.

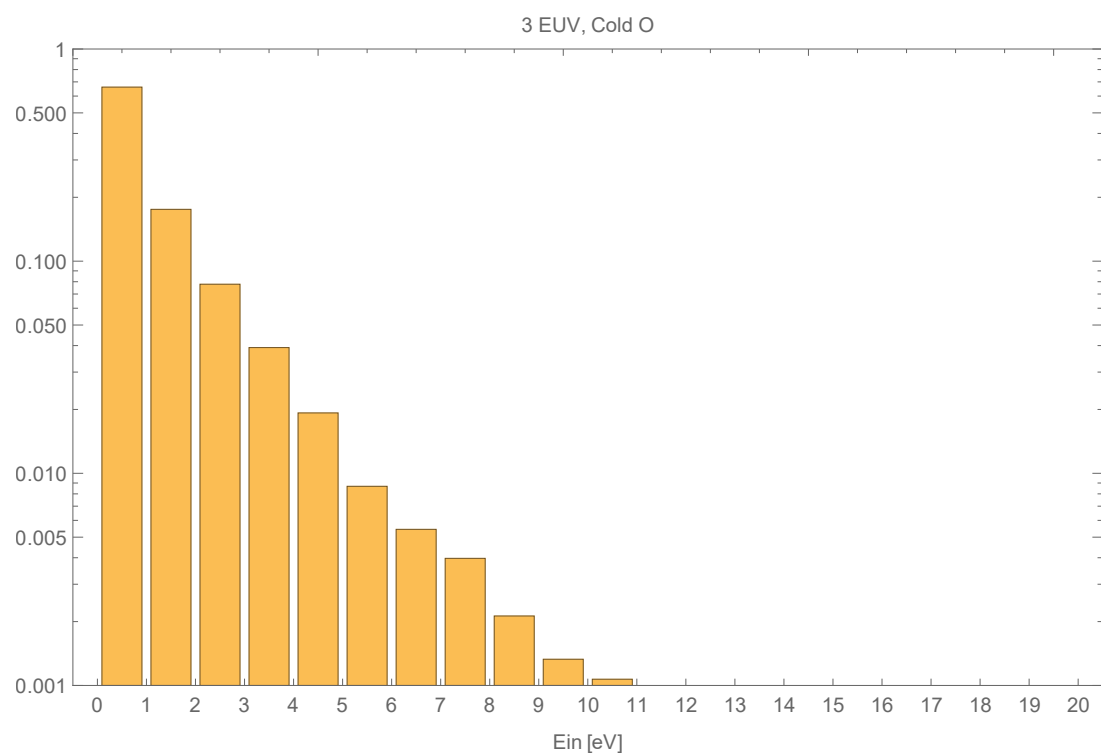


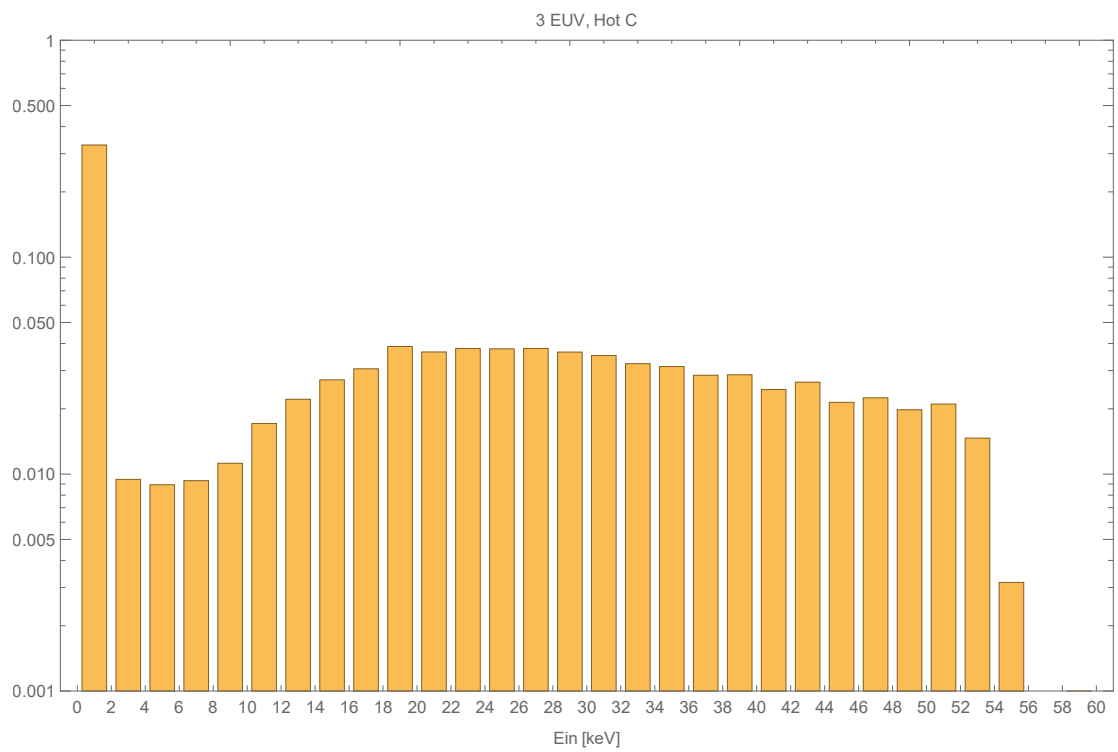


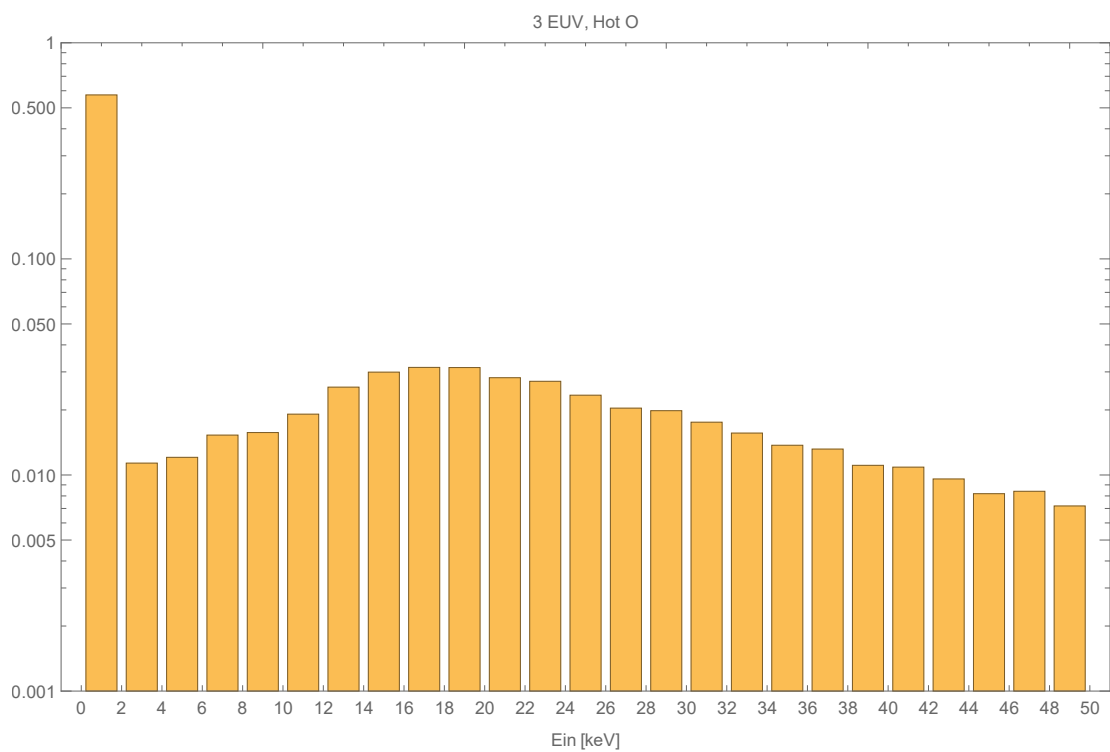


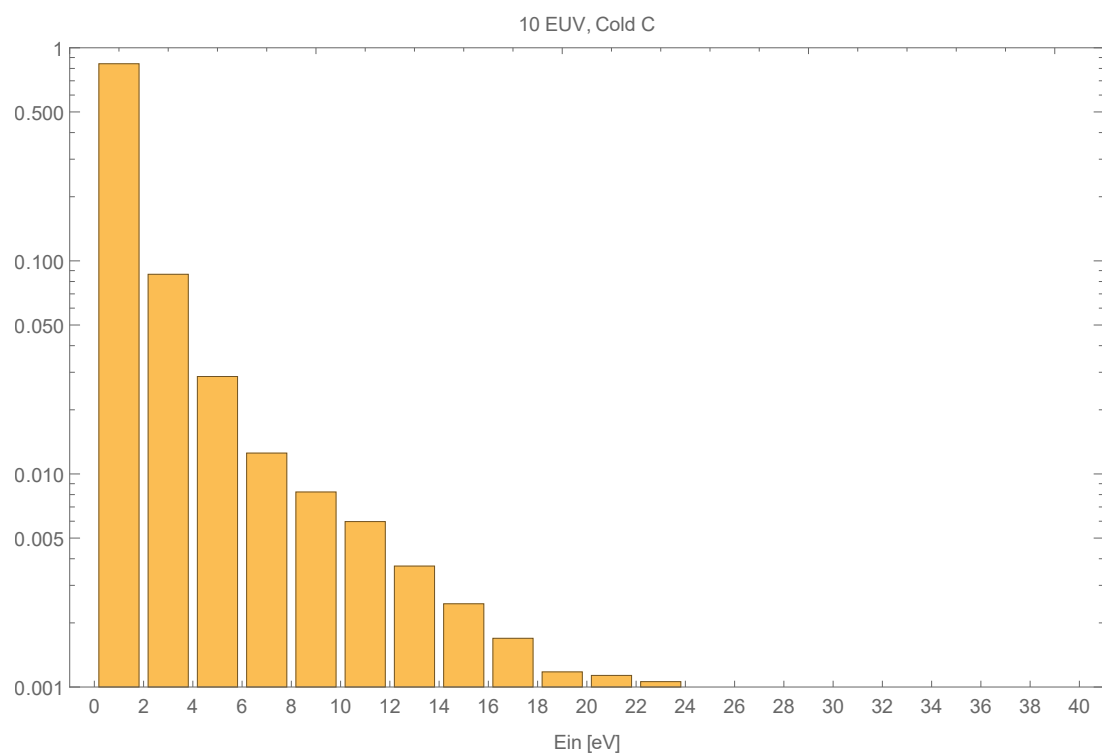


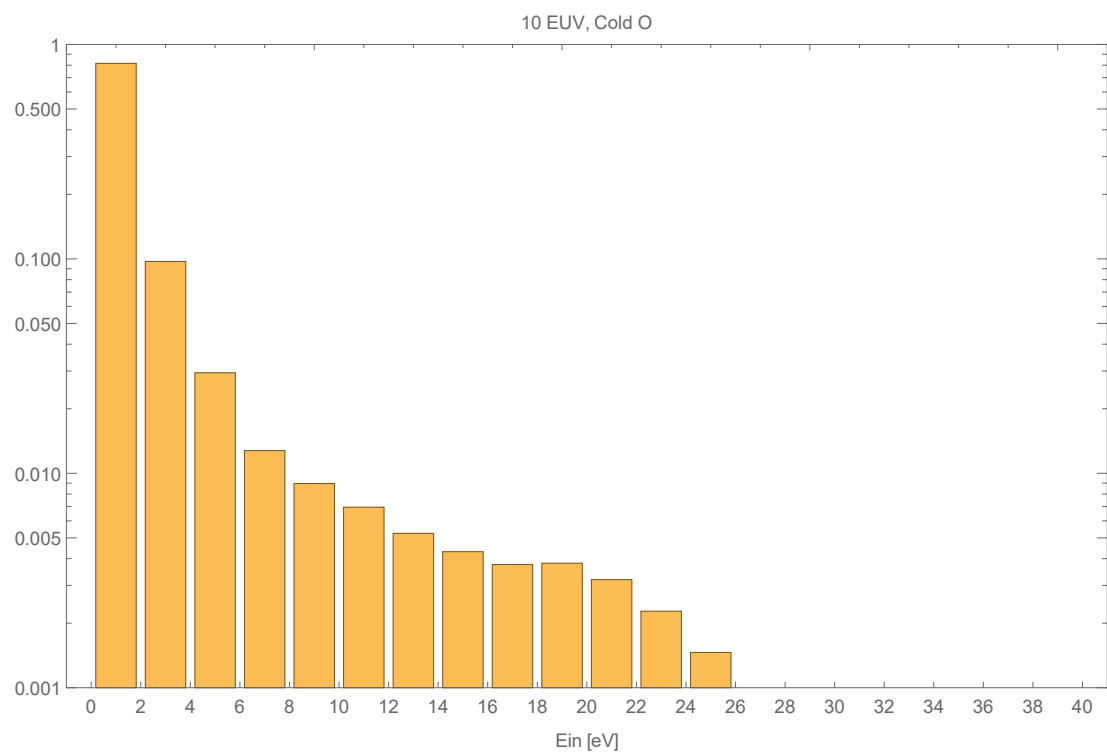


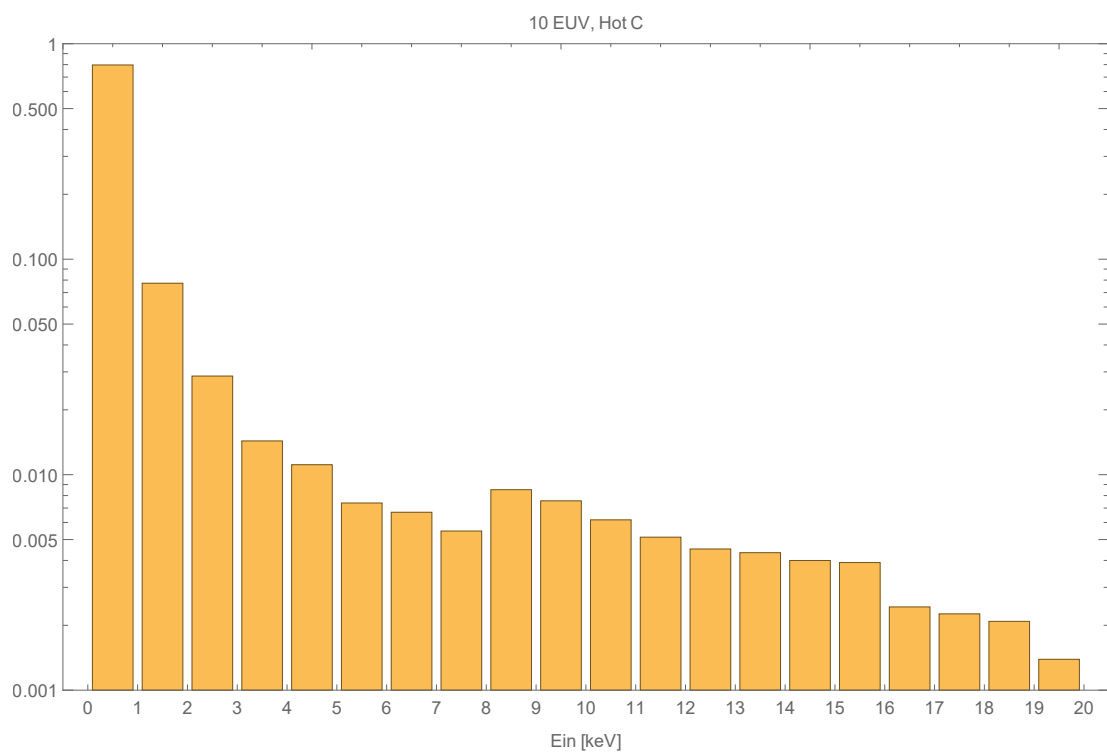


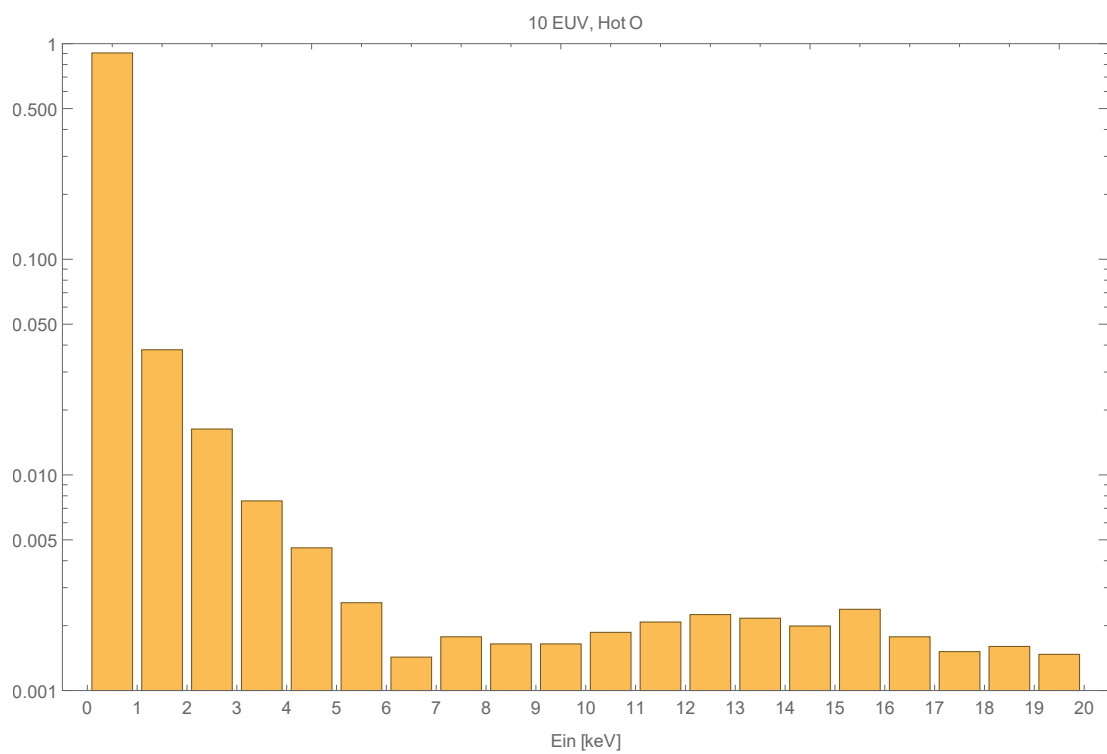












Yield: Incident cold C (1 EUV)

Species Out	M _{in} [amu]	M _{out} [amu]	σ_d [cm ²]	$\sigma(T>U_0)$ [cm ²]	α	P _{es}	θ [°]	S _n [eV cm ²]	U ₀ [eV]	E _{es} [eV]	E _{in} [eV]	Impact Rate [s ⁻¹]	Ys	Yc	Loss Rate [s ⁻¹]
C	12	12	2.94×10^{-15}	3.47×10^{-15}	0.2	0.5	52.50	1.10×10^{-14}	1.47	2.99	27.50	1.24×10^{23}	1.27	9.95×10^{-1}	6.77×10^{19}
CO2	12	44	2.11×10^{-15}	2.08×10^{-15}	0.2	0.5	52.50	1.33×10^{-14}	5.40	16.52	27.50	1.24×10^{23}	2.56	$3. \times 10^{-1}$	5.13×10^{22}
CO	12	28	2.31×10^{-15}	2.46×10^{-15}	0.2	0.5	52.50	1.35×10^{-14}	3.44	6.24	27.50	1.24×10^{23}	6.08×10^{-1}	3.33×10^{-1}	6.02×10^{21}
O	12	16	2.68×10^{-15}	3.09×10^{-15}	0.2	0.5	52.50	1.21×10^{-14}	1.96	3.86	27.50	1.24×10^{23}	1.27	9.05×10^{-1}	1.25×10^{23}
Ar36	12	36	2.19×10^{-15}	2.24×10^{-15}	0.2	0.5	52.50	1.35×10^{-14}	4.42	7.94	27.50	1.24×10^{23}	1.18	5.48×10^{-1}	2.47×10^{18}
Ar38	12	38	2.15×10^{-15}	2.14×10^{-15}	0.2	0.5	52.50	1.32×10^{-14}	4.66	8.49	27.50	1.24×10^{23}	1.19	5.17×10^{-1}	3.98×10^{17}

Yield: Incident cold O (1 EUV)

Species Out	M _{in} [amu]	M _{out} [amu]	σ_d [cm ²]	$\sigma(T>U_0)$ [cm ²]	α	P _{es}	θ [°]	S _n [eV cm ²]	U ₀ [eV]	E _{es} [eV]	E _{in} [eV]	Impact Rate [s ⁻¹]	Ys	Yc	Loss Rate [s ⁻¹]
O	16	16	2.91×10^{-15}	3.86×10^{-15}	0.2	0.5	53.26	1.49×10^{-14}	1.96	3.83	28.98	7.06×10^{24}	1.48	1.04	8.69×10^{24}
CO2	16	44	2.21×10^{-15}	2.63×10^{-15}	0.2	0.5	53.26	1.79×10^{-14}	5.40	10.17	28.98	7.06×10^{24}	7.74×10^{-1}	2.43×10^{-1}	1.07×10^{24}
CO	16	28	2.47×10^{-15}	3.13×10^{-15}	0.2	0.5	53.26	1.72×10^{-14}	3.44	6.20	28.98	7.06×10^{24}	7.09×10^{-1}	4.07×10^{-1}	4.27×10^{23}
C	16	12	3.18×10^{-15}	4.19×10^{-15}	0.2	0.5	53.26	1.35×10^{-14}	1.47	2.99	28.98	7.06×10^{24}	1.47	1.15	4.51×10^{21}
Ar36	16	36	2.32×10^{-15}	2.84×10^{-15}	0.2	0.5	53.26	1.78×10^{-14}	4.42	7.87	28.98	7.06×10^{24}	1.4	6.94×10^{-1}	1.77×10^{20}
Ar38	16	38	2.28×10^{-15}	2.72×10^{-15}	0.2	0.5	53.26	1.75×10^{-14}	4.66	8.36	28.98	7.06×10^{24}	1.4	6.62×10^{-1}	2.83×10^{19}

Yield: Incident hot C (1 EUV)

Species Out	M _{in} [amu]	M _{out} [amu]	σ_d [cm ²]	$\sigma(T>U_0)$ [cm ²]	α	P _{es}	θ [°]	S _n [eV cm ²]	U ₀ [eV]	E _{es} [eV]	E _{in} [eV]	Impact Rate [s ⁻¹]	Ys	Yc	Loss Rate [s ⁻¹]
C	12	12	2.29×10^{-15}	1.56×10^{-15}	0.2	0.5	50.70	1.42×10^{-14}	1.47	6.79	4623.20	6.83×10^{20}	6.18×10^{-1}	1.67	4.43×10^{17}
CO2	12	44	1.60×10^{-15}	8.92×10^{-16}	0.2	0.5	50.70	2.21×10^{-14}	5.40	20.63	4623.20	6.83×10^{20}	1.69×10^{-1}	3.28×10^{-1}	7.86×10^{19}
CO	12	28	1.77×10^{-15}	1.08×10^{-15}	0.2	0.5	50.70	1.99×10^{-14}	3.44	14.20	4623.20	6.83×10^{20}	2.78×10^{-1}	6.35×10^{-1}	4.61×10^{19}
O	12	16	2.08×10^{-15}	1.38×10^{-15}	0.2	0.5	50.70	1.63×10^{-14}	1.96	8.79	4623.20	6.83×10^{20}	6.08×10^{-1}	1.57	8.67×10^{20}
Ar36	12	36	1.67×10^{-15}	9.72×10^{-16}	0.2	0.5	50.70	2.12×10^{-14}	4.42	17.45	4623.20	6.83×10^{20}	5.27×10^{-1}	1.11	1.96×10^{16}
Ar38	12	38	1.63×10^{-15}	9.24×10^{-16}	0.2	0.5	50.70	2.04×10^{-14}	4.66	18.44	4623.20	6.83×10^{20}	5.19×10^{-1}	1.04	3.08×10^{15}

Yield: Incident hot O (1 EUV)

Species Out	M _{in} [amu]	M _{out} [amu]	σ_d [cm ²]	$\sigma(T>U_0)$ [cm ²]	α	P _{es}	θ [°]	S _n [eV cm ²]	U ₀ [eV]	E _{es} [eV]	E _{in} [eV]	Impact Rate [s ⁻¹]	Y _s	Y _c	Loss Rate [s ⁻¹]
O	16	16	2.34×10^{-15}	1.88×10^{-15}	0.2	0.5	50.31	2.45×10^{-14}	1.96	8.52	4274.80	4.13×10^{22}	7.56×10^{-1}	2.28	7.39×10^{22}
CO2	16	44	1.74×10^{-15}	1.22×10^{-15}	0.2	0.5	50.31	3.53×10^{-14}	5.40	20.53	4274.80	4.13×10^{22}	2.2×10^{-1}	5.41×10^{-1}	7.27×10^{21}
CO	16	28	1.96×10^{-15}	1.48×10^{-15}	0.2	0.5	50.31	3.10×10^{-14}	3.44	14.01	4274.80	4.13×10^{22}	3.54×10^{-1}	9.9×10^{-1}	4.14×10^{21}
C	16	12	2.57×10^{-15}	2.06×10^{-15}	0.2	0.5	50.31	2.13×10^{-14}	1.47	6.58	4274.80	4.13×10^{22}	7.51×10^{-1}	2.36	3.67×10^{19}
Ar36	16	36	1.83×10^{-15}	1.33×10^{-15}	0.2	0.5	50.31	3.35×10^{-14}	4.42	17.34	4274.80	4.13×10^{22}	6.8×10^{-1}	1.79	1.79×10^{18}
Ar38	16	38	1.79×10^{-15}	1.26×10^{-15}	0.2	0.5	50.31	3.25×10^{-14}	4.66	18.19	4274.80	4.13×10^{22}	6.6×10^{-1}	1.68	2.8×10^{17}

Yield: Incident cold C (3 EUV)

Species Out	M _{in} [amu]	M _{out} [amu]	σ_d [cm ²]	$\sigma(T>U_0)$ [cm ²]	α	P _{es}	θ [°]	S _n [eV cm ²]	U ₀ [eV]	E _{es} [eV]	E _{in} [eV]	Impact Rate [s ⁻¹]	Y _s	Y _c	Loss Rate [s ⁻¹]
C	12	12	3.40×10^{-15}	5.27×10^{-15}	0.2	0.5	53.96	4.13×10^{-15}	1.41	1.75	0.91	1.51×10^{25}	2.32	5.75×10^{-1}	5.57×10^{22}
CO2	12	44	2.28×10^{-15}	3.08×10^{-15}	0.2	0.5	53.96	5.71×10^{-15}	5.19	8.47	0.91	1.51×10^{25}	8.79×10^{-1}	1.29×10^{-1}	3.37×10^{21}
CO	12	28	2.66×10^{-15}	3.80×10^{-15}	0.2	0.5	53.96	5.23×10^{-15}	3.30	4.33	0.91	1.51×10^{25}	1.34	2.4×10^{-1}	6.4×10^{22}
O	12	16	3.11×10^{-15}	4.72×10^{-15}	0.2	0.5	53.96	4.62×10^{-15}	1.89	2.26	0.91	1.51×10^{25}	2.53	5.82×10^{-1}	5.3×10^{24}
Ar36	12	36	2.46×10^{-15}	3.37×10^{-15}	0.2	0.5	53.96	5.61×10^{-15}	4.24	6.44	0.91	1.51×10^{25}	2.85	5.08×10^{-1}	1.3×10^{19}
Ar38	12	38	2.37×10^{-15}	3.22×10^{-15}	0.2	0.5	53.96	5.62×10^{-15}	4.48	7.36	0.91	1.51×10^{25}	2.82	4.77×10^{-1}	1.56×10^{18}

Yield: Incident cold O (3 EUV)

Species Out	M _{in} [amu]	M _{out} [amu]	σ_d [cm ²]	$\sigma(T>U_0)$ [cm ²]	α	P _{es}	θ [°]	S _n [eV cm ²]	U ₀ [eV]	E _{es} [eV]	E _{in} [eV]	Impact Rate [s ⁻¹]	Y _s	Y _c	Loss Rate [s ⁻¹]
O	16	16	3.31×10^{-15}	5.61×10^{-15}	0.2	0.5	52.70	5.13×10^{-15}	1.89	2.28	1.12	1.17×10^{26}	2.79	6.38×10^{-1}	6.61×10^{25}
CO2	16	44	2.44×10^{-15}	3.72×10^{-15}	0.2	0.5	52.70	7.20×10^{-15}	5.19	7.10	1.12	1.17×10^{26}	9.72×10^{-1}	1.44×10^{-1}	4.28×10^{22}
CO	16	28	2.82×10^{-15}	4.54×10^{-15}	0.2	0.5	52.70	6.29×10^{-15}	3.30	3.86	1.12	1.17×10^{26}	1.51	2.86×10^{-1}	8.05×10^{23}
C	16	12	3.63×10^{-15}	6.19×10^{-15}	0.2	0.5	52.70	4.50×10^{-15}	1.41	1.75	1.12	1.17×10^{26}	2.52	6.15×10^{-1}	6.46×10^{23}
Ar36	16	36	2.61×10^{-15}	4.06×10^{-15}	0.2	0.5	52.70	6.87×10^{-15}	4.24	5.23	1.12	1.17×10^{26}	2.92	5.2×10^{-1}	1.59×10^{20}
Ar38	16	38	2.56×10^{-15}	3.89×10^{-15}	0.2	0.5	52.70	6.95×10^{-15}	4.48	5.66	1.12	1.17×10^{26}	2.9	5.19×10^{-1}	1.92×10^{19}

Yield: Incident hot C (3 EUV)

Species Out	M _{in} [amu]	M _{out} [amu]	σ_d [cm ²]	$\sigma(T>U_0)$ [cm ²]	α	P _{es}	θ [°]	S _n [eV cm ²]	U ₀ [eV]	E _{es} [eV]	E _{in} [eV]	Impact Rate [s ⁻¹]	Y _s	Y _c	Loss Rate [s ⁻¹]
C	12	12	1.88 × 10 ⁻¹⁵	6.41 × 10 ⁻¹⁶	0.2	0.5	52.10	8.52 × 10 ⁻¹⁵	1.41	10.07	19659.00	6.06 × 10 ²³	2.98 × 10 ⁻¹	2.02	7.95 × 10 ²¹
CO2	12	44	1.24 × 10 ⁻¹⁵	2.14 × 10 ⁻¹⁶	0.2	0.5	52.10	1.85 × 10 ⁻¹⁴	5.19	31.31	19659.00	6.06 × 10 ²³	5.73 × 10 ⁻²	6.06 × 10 ⁻¹	3.87 × 10 ²¹
CO	12	28	1.39 × 10 ⁻¹⁵	3.01 × 10 ⁻¹⁶	0.2	0.5	52.10	1.47 × 10 ⁻¹⁴	3.30	21.64	19659.00	6.06 × 10 ²³	1.06 × 10 ⁻¹	1.02	2.68 × 10 ²²
O	12	16	1.68 × 10 ⁻¹⁵	4.90 × 10 ⁻¹⁶	0.2	0.5	52.10	1.04 × 10 ⁻¹⁴	1.89	13.19	19659.00	6.06 × 10 ²³	2.7 × 10 ⁻¹	2.09	1.02 × 10 ²⁴
Ar36	12	36	1.30 × 10 ⁻¹⁵	2.38 × 10 ⁻¹⁶	0.2	0.5	52.10	1.69 × 10 ⁻¹⁴	4.24	26.71	19659.00	6.06 × 10 ²³	1.84 × 10 ⁻¹	1.94	9.43 × 10 ¹⁸
Ar38	12	38	1.26 × 10 ⁻¹⁵	2.21 × 10 ⁻¹⁶	0.2	0.5	52.10	1.61 × 10 ⁻¹⁴	4.48	27.94	19659.00	6.06 × 10 ²³	1.79 × 10 ⁻¹	1.8	1.22 × 10 ¹⁸

Yield: Incident hot O (3 EUV)

Species Out	M _{in} [amu]	M _{out} [amu]	σ_d [cm ²]	$\sigma(T>U_0)$ [cm ²]	α	P _{es}	θ [°]	S _n [eV cm ²]	U ₀ [eV]	E _{es} [eV]	E _{in} [eV]	Impact Rate [s ⁻¹]	Y _s	Y _c	Loss Rate [s ⁻¹]
O	16	16	2.15 × 10 ⁻¹⁵	1.44 × 10 ⁻¹⁵	0.2	0.5	52.15	1.86 × 10 ⁻¹⁴	1.89	11.10	10442.00	2.05 × 10 ²³	7.2 × 10 ⁻¹	2.69	3.88 × 10 ²³
CO2	16	44	1.45 × 10 ⁻¹⁵	4.92 × 10 ⁻¹⁶	0.2	0.5	52.15	3.50 × 10 ⁻¹⁴	5.19	29.80	10442.00	2.05 × 10 ²³	1.14 × 10 ⁻¹	8.56 × 10 ⁻¹	1.31 × 10 ²¹
CO	16	28	1.70 × 10 ⁻¹⁵	8.04 × 10 ⁻¹⁶	0.2	0.5	52.15	2.74 × 10 ⁻¹⁴	3.30	19.59	10442.00	2.05 × 10 ²³	2.53 × 10 ⁻¹	1.39	9.54 × 10 ²¹
C	16	12	2.45 × 10 ⁻¹⁵	1.85 × 10 ⁻¹⁵	0.2	0.5	52.15	1.49 × 10 ⁻¹⁴	1.41	8.19	10442.00	2.05 × 10 ²³	7.73 × 10 ⁻¹	2.54	3.12 × 10 ²¹
Ar36	16	36	1.55 × 10 ⁻¹⁵	5.95 × 10 ⁻¹⁶	0.2	0.5	52.15	3.18 × 10 ⁻¹⁴	4.24	25.04	10442.00	2.05 × 10 ²³	3.92 × 10 ⁻¹	2.69	3.24 × 10 ¹⁸
Ar38	16	38	1.50 × 10 ⁻¹⁵	5.48 × 10 ⁻¹⁶	0.2	0.5	52.15	3.06 × 10 ⁻¹⁴	4.48	26.15	10442.00	2.05 × 10 ²³	3.66 × 10 ⁻¹	2.52	4.18 × 10 ¹⁷

Yield: Incident cold C (10 EUV)

Species Out	M _{in} [amu]	M _{out} [amu]	σ_d [cm ²]	$\sigma(T>U_0)$ [cm ²]	α	P _{es}	θ [°]	S _n [eV cm ²]	U ₀ [eV]	E _{es} [eV]	E _{in} [eV]	Impact Rate [s ⁻¹]	Y _s	Y _c	Loss Rate [s ⁻¹]
C	12	12	3.39 × 10 ⁻¹⁵	5.07 × 10 ⁻¹⁵	0.2	0.5	60.03	5.20 × 10 ⁻¹⁵	1.28	1.81	3.60	1.13 × 10 ²⁶	2.37	8.75 × 10 ⁻¹	1.15 × 10 ²⁵
CO2	12	44	2.33 × 10 ⁻¹⁵	2.93 × 10 ⁻¹⁵	0.2	0.5	60.03	7.46 × 10 ⁻¹⁵	4.71	7.76	3.60	1.13 × 10 ²⁶	7.65 × 10 ⁻¹	1.76 × 10 ⁻¹	1.61 × 10 ²¹
CO	12	28	2.65 × 10 ⁻¹⁵	3.60 × 10 ⁻¹⁵	0.2	0.5	60.03	6.85 × 10 ⁻¹⁵	3.00	4.03	3.60	1.13 × 10 ²⁶	1.13	3.24 × 10 ⁻¹	3.06 × 10 ²³
O	12	16	3.11 × 10 ⁻¹⁵	4.57 × 10 ⁻¹⁵	0.2	0.5	60.03	5.76 × 10 ⁻¹⁵	1.71	2.34	3.60	1.13 × 10 ²⁶	2.33	8.02 × 10 ⁻¹	5.5 × 10 ²⁵
Ar36	12	36	2.48 × 10 ⁻¹⁵	3.21 × 10 ⁻¹⁵	0.2	0.5	60.03	7.24 × 10 ⁻¹⁵	3.85	6.46	3.60	1.13 × 10 ²⁶	2.35	6.01 × 10 ⁻¹	3.17 × 10 ²⁰
Ar38	12	38	2.43 × 10 ⁻¹⁵	3.07 × 10 ⁻¹⁵	0.2	0.5	60.03	7.21 × 10 ⁻¹⁵	4.07	6.78	3.60	1.13 × 10 ²⁶	2.3	5.8 × 10 ⁻¹	3.4 × 10 ¹⁹

Neutral Profiles (10 EUV), Exobase altitude: 750 km

O [cm ⁻³]	CO2 [cm ⁻³]	CO [cm ⁻³]	C [cm ⁻³]	Ar36 [cm ⁻³]	Ar38 [cm ⁻³]	T [K]	O [%]	CO2 [%]	CO [%]	C [%]	Ar36 [%]	Ar38 [%]
1.46 × 10 ⁷	4510.00	315000.00	2.38 × 10 ⁶	218.00	25.60	806	84.394266	0.026070	1.820835	13.757421	0.001260	0.000148

Yield: Incident hot C (10 EUV)

Species Out	M _{in} [amu]	M _{out} [amu]	σ_d [cm ²]	$\sigma(T>U_0)$ [cm ²]	α	P _{es}	θ [°]	S _n [eV cm ²]	U ₀ [eV]	E _{es} [eV]	E _{in} [eV]	Impact Rate [s ⁻¹]	Y _s	Y _c	Loss Rate [s ⁻¹]
C	12	12	2.39×10^{-15}	1.66×10^{-15}	0.2	0.5	54.40	1.54×10^{-14}	1.28	6.05	7358.10	3.77×10^{24}	8.57×10^{-1}	1.72	9.08×10^{23}
CO2	12	44	1.60×10^{-15}	7.64×10^{-16}	0.2	0.5	54.40	2.44×10^{-14}	4.71	19.04	7358.10	3.77×10^{24}	1.76×10^{-1}	2.97×10^{-1}	2.65×10^{20}
CO	12	28	1.80×10^{-15}	1.01×10^{-15}	0.2	0.5	54.40	2.19×10^{-14}	3.00	13.08	7358.10	3.77×10^{24}	3.07×10^{-1}	5.78×10^{-1}	3.68×10^{22}
O	12	16	2.16×10^{-15}	1.44×10^{-15}	0.2	0.5	54.40	1.77×10^{-14}	1.71	7.89	7358.10	3.77×10^{24}	7.87×10^{-1}	1.53	4.84×10^{24}
Ar36	12	36	1.69×10^{-15}	8.62×10^{-16}	0.2	0.5	54.40	2.34×10^{-14}	3.85	16.12	7358.10	3.77×10^{24}	5.6×10^{-1}	1.01	4.37×10^{19}
Ar38	12	38	1.65×10^{-15}	8.07×10^{-16}	0.2	0.5	54.40	2.26×10^{-14}	4.07	16.87	7358.10	3.77×10^{24}	5.29×10^{-1}	9.43×10^{-1}	4.77×10^{18}

Yield: Incident hot O (10 EUV)

Species Out	M _{in} [amu]	M _{out} [amu]	σ_d [cm ²]	$\sigma(T>U_0)$ [cm ²]	α	P _{es}	θ [°]	S _n [eV cm ²]	U ₀ [eV]	E _{es} [eV]	E _{in} [eV]	Impact Rate [s ⁻¹]	Y _s	Y _c	Loss Rate [s ⁻¹]
O	16	16	2.76×10^{-15}	3.22×10^{-15}	0.2	0.5	56.60	1.89×10^{-14}	1.71	5.47	2058.90	1.61×10^{24}	1.63	2.22	2.59×10^{24}
CO2	16	44	1.98×10^{-15}	1.82×10^{-15}	0.2	0.5	56.60	2.97×10^{-14}	4.71	14.90	2058.90	1.61×10^{24}	3.81×10^{-1}	4.94×10^{-1}	1.31×10^{20}
CO	16	28	2.27×10^{-15}	2.39×10^{-15}	0.2	0.5	56.60	2.50×10^{-14}	3.00	9.64	2058.90	1.61×10^{24}	7.04×10^{-1}	9.52×10^{-1}	2.01×10^{22}
C	16	12	3.07×10^{-15}	3.70×10^{-15}	0.2	0.5	56.60	1.58×10^{-14}	1.28	4.08	2058.90	1.61×10^{24}	1.8	2.32	4.92×10^{23}
Ar36	16	36	2.10×10^{-15}	2.04×10^{-15}	0.2	0.5	56.60	2.78×10^{-14}	3.85	12.30	2058.90	1.61×10^{24}	1.2	1.62	2.17×10^{19}
Ar38	16	38	2.05×10^{-15}	1.94×10^{-15}	0.2	0.5	56.60	2.72×10^{-14}	4.07	12.95	2058.90	1.61×10^{24}	1.16	1.54	2.39×10^{18}

Yield: Incident cold C (10 EUV)

Species Out	M _{in} [amu]	M _{out} [amu]	σ_d [cm ²]	$\sigma(T>U_0)$ [cm ²]	α	P _{es}	θ [°]	S _n [eV cm ²]	U ₀ [eV]	E _{es} [eV]	E _{in} [eV]	Impact Rate [s ⁻¹]	Y _s	Y _c	Loss Rate [s ⁻¹]
C	12	12	3.39×10^{-15}	5.07×10^{-15}	0.2	0.5	60.03	5.20×10^{-15}	1.28	1.81	3.60	1.13×10^{26}	2.37	8.75×10^{-1}	1.15×10^{25}
CO2	12	44	2.33×10^{-15}	2.93×10^{-15}	0.2	0.5	60.03	7.46×10^{-15}	4.71	7.76	3.60	1.13×10^{26}	7.65×10^{-1}	1.76×10^{-1}	1.61×10^{21}
CO	12	28	2.65×10^{-15}	3.60×10^{-15}	0.2	0.5	60.03	6.85×10^{-15}	3.00	4.03	3.60	1.13×10^{26}	1.13	3.24×10^{-1}	3.06×10^{23}
O	12	16	3.11×10^{-15}	4.57×10^{-15}	0.2	0.5	60.03	5.76×10^{-15}	1.71	2.34	3.60	1.13×10^{26}	2.33	8.02×10^{-1}	5.5×10^{25}
Ar36	12	36	2.48×10^{-15}	3.21×10^{-15}	0.2	0.5	60.03	7.24×10^{-15}	3.85	6.46	3.60	1.13×10^{26}	2.35	6.01×10^{-1}	3.17×10^{20}
Ar38	12	38	2.43×10^{-15}	3.07×10^{-15}	0.2	0.5	60.03	7.21×10^{-15}	4.07	6.78	3.60	1.13×10^{26}	2.3	5.8×10^{-1}	3.4×10^{19}

Neutral Profiles (1 EUV, Exobase altitude: 220 km)

O [cm ⁻³]	CO2 [cm ⁻³]	CO [cm ⁻³]	C [cm ⁻³]	Ar36 [cm ⁻³]	Ar38 [cm ⁻³]	T [K]	O [%]	CO2 [%]	CO [%]	C [%]	Ar36 [%]	Ar38 [%]
3.42×10^7	1.50×10^7	4.59×10^6	16200.00	1110.00	185.00	222	63.559919	27.877157	8.530410	0.030107	0.002063	0.000344

Neutral Profiles (3 EUV), Exobase altitude: 370 km

O [cm ⁻³]	CO2 [cm ⁻³]	CO [cm ⁻³]	C [cm ⁻³]	Ar36 [cm ⁻³]	Ar38 [cm ⁻³]	T [K]	O [%]	CO2 [%]	CO [%]	C [%]	Ar36 [%]	Ar38 [%]
3.50 × 10 ⁷	501000.00	2.01 × 10 ⁶	272000.00	380.00	52.70	416	92.633193	1.325978	5.319792	0.719892	0.001006	0.000139

Neutral Profiles (10 EUV), Exobase altitude: 750 km

O [cm ⁻³]	CO2 [cm ⁻³]	CO [cm ⁻³]	C [cm ⁻³]	Ar36 [cm ⁻³]	Ar38 [cm ⁻³]	T [K]	O [%]	CO2 [%]	CO [%]	C [%]	Ar36 [%]	Ar38 [%]
1.46 × 10 ⁷	4510.00	315000.00	2.38 × 10 ⁶	218.00	25.60	806	84.394266	0.026070	1.820835	13.757421	0.001260	0.000148